



AFRL-AFOSR-VA-TR-2016-0359

**Signal Processing, Pattern Formation and Adaptation in Neural
Oscillators**

**Edward Large
Circular Logic LLC
399 NW 7TH Avenue
Boca Raton, FL 33486-3509**

**11/29/2016
Final Report**

DISTRIBUTION A: Distribution approved for public release.

Air Force Research Laboratory
AF Office Of Scientific Research (AFOSR)/RTB2

REPORT DOCUMENTATION PAGE			Form Approved OMB No. 0704-0188	
<p>The public reporting burden for this collection of information is estimated to average 1 hour per response, including the time for reviewing instructions, searching existing data sources, gathering and maintaining the data needed, and completing and reviewing the collection of information. Send comments regarding this burden estimate or any other aspect of this collection of information, including suggestions for reducing the burden, to Department of Defense, Executive Services, Directorate (0704-0188). Respondents should be aware that notwithstanding any other provision of law, no person shall be subject to any penalty for failing to comply with a collection of information if it does not display a currently valid OMB control number.</p> <p>PLEASE DO NOT RETURN YOUR FORM TO THE ABOVE ORGANIZATION.</p>				
1. REPORT DATE (DD-MM-YYYY) 29-11-2016		2. REPORT TYPE Final Performance	3. DATES COVERED (From - To) 01 Aug 2012 to 31 Jul 2016	
4. TITLE AND SUBTITLE Signal Processing, Pattern Formation and Adaptation in Neural Oscillators			5a. CONTRACT NUMBER	
			5b. GRANT NUMBER FA9550-12-1-0388	
			5c. PROGRAM ELEMENT NUMBER 61102F	
6. AUTHOR(S) Edward Large			5d. PROJECT NUMBER	
			5e. TASK NUMBER	
			5f. WORK UNIT NUMBER	
7. PERFORMING ORGANIZATION NAME(S) AND ADDRESS(ES) Circular Logic LLC 399 NW 7TH Avenue Boca Raton, FL 33486-3509 US			8. PERFORMING ORGANIZATION REPORT NUMBER	
9. SPONSORING/MONITORING AGENCY NAME(S) AND ADDRESS(ES) AF Office of Scientific Research 875 N. Randolph St. Room 3112 Arlington, VA 22203			10. SPONSOR/MONITOR'S ACRONYM(S) AFRL/AFOSR RTB2	
			11. SPONSOR/MONITOR'S REPORT NUMBER(S) AFRL-AFOSR-VA-TR-2016-0359	
12. DISTRIBUTION/AVAILABILITY STATEMENT DISTRIBUTION A: Distribution approved for public release.				
13. SUPPLEMENTARY NOTES				
14. ABSTRACT <p>In this project, we developed a theoretical framework for auditory neural processing and auditory perception. We modeled the auditory system as a dynamical system consisting of oscillatory networks, and auditory perception as stable dynamic patterns formed in the networks in response to acoustic signals. We developed GrFNNS, generic models that capture the neurocomputational properties of a family of neurophysiological models using bifurcation theory. We conducted theoretical analyses of GrFNNS and made significant progress in understanding the signal processing, pattern formation and plasticity in them. We developed three models that exploit these properties to model important aspects of auditory neurophysiology and auditory perception: a model of cochlear dynamics, a model of mode-locked neural oscillation in the human auditory brainstem, and a model of cortical phase locking to auditory rhythms. Future modeling efforts based on canonical dynamical systems could bring us closer to understanding fundamental mechanisms of hearing, communication, and auditory system development</p>				
15. SUBJECT TERMS Nonlinear Dynamics, Auditory Perception, Neural Oscillators				
16. SECURITY CLASSIFICATION OF:		17. LIMITATION OF ABSTRACT	18. NUMBER OF PAGES	19a. NAME OF RESPONSIBLE PERSON
a. REPORT Unclassified	b. ABSTRACT Unclassified	c. THIS PAGE Unclassified	UU	BRADSHAW, PATRICK
Standard Form 298 (Rev. 8/98) Prescribed by ANSI Std. Z39.18				

DISTRIBUTION A: Distribution approved for public release.

				19b. TELEPHONE NUMBER (Include area code) 703-588-8492
--	--	--	--	--

Standard Form 298 (Rev. 8/98)
Prescribed by ANSI Std. Z39.18

DISTRIBUTION A: Distribution approved for public release.

AFOSR Final Performance Report

Project Title: Signal Processing, Pattern Formation and Adaptation in Neural Oscillators

Award Number: FA9550-12-10388

Start Date:

Program Manager: Dr. Patrick O. Bradshaw

Sensory Information Systems Program
Air Force Office of Scientific Research^[L]
Directorate of Chemistry and Biological Sciences
875 North Randolph Street
Suite 325^[L]
Arlington, Virginia 22203-1768
E-mail: patrick.bradshaw.3@us.af.mil
Phone: (703) 588-8492
Fax: FAX (703) 696-7360

Principal Investigator: Dr. Edward W. Large
President
Circular Logic, LLC
222 Pitkin Street
East Hartford, CT 06108
E-mail: edward.large@circular-logic.com
Phone: (860) 282-4215
Fax: (860) 282-4901

Accomplishments/New Findings:

- We developed a nonlinear dynamical systems approach to auditory processing using gradient frequency networks of neural oscillators. Oscillators in the network are driven by external forcing and receive input from other oscillators. Both types of interaction may involve linear and/or nonlinear coupling, which can evolve over time via a generalized form of Hebbian plasticity.
- We conducted three types of theoretical analyses to understand signal processing, pattern formation and adaptation in networks of neural oscillators. First, we analyzed and categorized the driven behaviors of canonical oscillators under periodic forcing in four parameter regimes.
- Second, we analyzed coupled oscillators for each parameter regime identified in the previous study. These studies of systems of coupled oscillators enabled us to better understand and utilize the complex pattern forming dynamics of GrFNNs.
- Third, we completed several studies of Hebbian plasticity in gradient frequency neural networks. We expanded a single-frequency network with linear learning rule into a multi-frequency network with a nonlinear learning rule. We discovered a set of rich dynamics that are not observed in either single-frequency systems or systems without plasticity. We analyzed the dynamics of two simple oscillator systems with plastic connections: an oscillator with plastic coupling to single external input and two oscillators connected by plastic coupling.
- We developed a computational modeling framework for gradient frequency neural networks in Matlab®: the GrFNN (pronounced *griffin*) Toolbox. The toolbox was developed collaboration with the Music Dynamics Laboratory at UConn and has been released to the research community: <https://github.com/MusicDynamicsLab/GrFNNTToolbox>.
- We subcontracted with ArrayFire to speed up our computational simulations using GPU acceleration.
- We developed a C++ version of the gradient frequency neural network code that functions as an application program interface (API). It can be used to develop end-user applications that run on CPUs, GPU, mobile platforms and embedded devices.
- Next, we developed three models of auditory processing. First, we developed and analyzed a model of cochlear dynamics based on coupling between linear mechanical resonance of the basilar membrane and critical nonlinear oscillations of outer hair cells. We obtained analytical forms for auditory tuning curves of both unidirectionally and bidirectionally coupled systems. The tuning curves of the model fit auditory nerve tuning curve data from the macaque monkey well.
- We developed a canonical model of mode-locked neural oscillation in the human auditory brainstem. We showed that the model could reproduce frequency following responses (FFRs) to musical intervals recorded noninvasively in humans.
- We developed a model of cortical phase locking to auditory rhythms. We successfully tested the model's predictions in behavioral and neurophysiological experiments.

Summary:

Many systems in nature, especially biological systems, are nonlinear dynamical systems. Auditory perception provides a stunning example of just how powerful such systems can be. Humans recognize complex acoustic patterns under challenging listening conditions, such as a voice in a crowded room or on a city street. We quickly learn patterns that are significant to us, such as the sound of a new dog's bark or the rhythm of a samba. We segregate sounds from one another, so that we can attend to one sound while suppressing others. These and other remarkable capabilities of human perception arise from nonlinear dynamical processes in the auditory system.

We have developed a theoretical framework for auditory neural processing and auditory perception. Our approach models the auditory system as a dynamical system consisting of oscillatory neural networks, and auditory perception as stable dynamic patterns formed in the networks in response to acoustic signals. Our models capture neural dynamics using canonical dynamical systems. Canonical systems are not detailed neurophysiological models; they are generic models that capture the neurocomputational properties of a family of neurophysiological models using bifurcation theory. Such models apply across temporal and spatial scales. For example, they are appropriate for describing critical nonlinear oscillations of outer hair cells in the cochlea, mode-locking of chopper cells to sound in the cochlear nucleus, and entrainment of cortical oscillations to auditory rhythms.

We have made significant theoretical advances in understanding how gradient frequency neural networks (GrFNNs) respond to acoustic stimulation and how such networks can learn and adapt through Hebbian plasticity. We analyzed and categorized the driven behaviors of canonical oscillators under periodic forcing. We conducted series of studies of systems of coupled oscillators to better understand and utilize the complex network dynamics of GrFNNs. We completed a comprehensive study of Hebbian plasticity in gradient frequency neural networks. We discovered a set of rich dynamics that are not observed in either single-frequency systems or systems without plasticity.

We created a computational modeling framework in Matlab, called the GrFNN Toolbox, and we have made our models publicly available. We have developed C++ versions of the gradient frequency neural network code that can be used to develop end-user applications to run on CPUs, GPUs, mobile platforms and embedded devices. We have shown that our models can predict and explain various aspects of auditory processing and perception that are difficult to account for by more traditional models based on linear signal processing techniques.

We began development of three important classes of auditory models. First, we developed and analyzed a canonical model of cochlear dynamics based on coupling between linear mechanical resonance of the basilar membrane and critical nonlinear oscillations in the organ of Corti. To validate this model we compared it with auditory-nerve tuning-curve data from the macaque monkey. Second, we developed a canonical model of mode-locked neural oscillation in the human auditory brainstem. The model successfully predicted complex nonlinear population responses to musical intervals. Third, we developed a model of cortical phase locking to auditory rhythms. The model predicted the results of behavioral and neurophysiological experiments.

Our models are consistent with neurophysiological evidence on the role of neural oscillation at various levels of the auditory system, and they explain phenomena that other computational models fail to explain. The predictions hold for an entire family of dynamical systems, not only specific physiological systems. Thus, our model provides a theoretical and computational framework for the next generation of auditory processing devices.

1. Neural Processing at Multiple Timescales

Many systems in nature, especially biological systems, are nonlinear dynamical systems. This report describes an approach to auditory modeling using canonical dynamical systems. *Canonical systems* are not detailed neurophysiological models; they are *generic models that capture the computational properties of a family of neurophysiological models using bifurcation theory*. Our model captures the responses of oscillatory neural systems driven with time varying external signals (Large, Almonte, & Velasco, 2010). It is applicable across temporal and spatial scales, from pitches to pitch sequences to rhythmic patterns. As such, our models are appropriate for describing various phenomena in the auditory system, including critical nonlinear oscillations of outer hair cells (e.g., Fredrickson-Hemsing, Ji, Bruinsma, & Bozovic, 2012), mode-locking of choppers in the cochlear nucleus (e.g., Laudanski, Coombes, Palmer, & Sumner, 2010), and entrainment of oscillations in auditory cortex (e.g., S. Nozaradan, Peretz, Missal, & Mouraux, 2011).

This report is organized as follows. The remainder of Section 1 provides a brief introduction to gradient frequency neural networks, our canonical model for auditory dynamics. Sections 2 – 4 then describe a comprehensive set of studies that we carried out to understand the signal processing, pattern formation and adaptive properties of GrFNNs. Section 2 analyses signal processing properties. Section 3 analyzes the properties of coupled systems of oscillators, focusing on mode-locking, which enables complex patterns to form in the networks when stimulated with sound. Section 4 analyses plasticity in canonical oscillators, finding a set of rich dynamics that are not observed in either single-frequency systems or systems without plasticity. Finally, in Section 5 we describe three modeling projects that show how well our models can capture auditory processing at various temporal and spatial scales.

1.1. Gradient Frequency Neural Networks (GrFNNs)

Gradient frequency neural oscillator networks (GrFNNs) are canonical neural oscillators arrayed along a tonotopic frequency gradient, like filter banks (Patterson et al., 1992). Unlike filter banks, however, GrFNNs have nonlinear properties that are appropriate to model networks of spiking neurons (e.g., Hodgkin & Huxley, 1952) or mean-field descriptions of neural populations (e.g., Wilson & Cowan, 1972) near a Hopf or a Bautin bifurcation (Hoppensteadt & Izhikevich, 2001). Dynamical properties associated with these bifurcations have been identified in the auditory system (e.g., Fredrickson-Hemsing et al., 2012; Laudanski et al., 2010).

Our *canonical model* (Eq. 1) captures the dynamical properties of a network of neural oscillators driven with an acoustic signal, $x(t)$, and synaptic connections, c_{ij} , between all possible pairs of oscillators.

$$\tau_i \dot{z}_i = z_i \left(\alpha + i2\pi + \beta_1 + |z_i|^2 + \frac{\epsilon\beta_2 + |z_i|^4}{1 - \epsilon|z_i|^2} \right) + \sum_{j \neq i} c_{ij} \frac{z_j}{1 - \sqrt{\epsilon}z_j} \cdot \frac{1}{1 - \sqrt{\epsilon}z_i} + \frac{x(t)}{1 - \sqrt{\epsilon}x(t)} \cdot \frac{1}{1 - \sqrt{\epsilon}z_i} \quad (1)$$

where z_i is a *complex-valued state variable* that represents the amplitude and phase of the i th oscillator in the network, and the overdot denotes time derivative, and the roman i is the imaginary unit. The time constant, τ_i , determines the natural frequency, $\tau_i = 1/f_i$. The right-hand side of Equation 1 consists of intrinsic terms (all before the summation) and input terms from coupling within the network and external drive $x_i(t)$ (all after the summation). Depending on the parameter values, α , β_1 , β_2 and ϵ , a canonical oscillator exhibits one of several distinct intrinsic behaviors available near a *Hopf* bifurcation or a *Bautin* (a.k.a. double limit cycle) bifurcation. Stability analysis shows that there are four parameter regimes for canonical oscillators, each with a distinct set of autonomous and driven behaviors (Kim & Large, 2015) (see Section 2).

One key difference between the response of nonlinear oscillators and the response of linear bandpass filters is that individual oscillations *mode-lock* to periodic stimuli. Mode-locking means that k cycles of an oscillation lock to m cycles of the stimulus, where k and m are integers, as shown in Fig 1.1b ($k = m = 1$ is called phase-locking). Frequency (of the stimulus relative to the oscillation) and coupling strength determine the locking mode (Fig 1.1b). Mode-locking responses in an active oscillatory network produce frequencies that are not present in its stimulus: harmonics, subharmonics, integer ratios, and combinations of stimulus frequencies (Fig 1.1b). This predicts certain types of network interactions could carry out complex computations needed to explain the perception of structure, for example the perception of pitch at event timescales (Meddis & O'Mard, 2006) and the perception of pulse and meter at rhythmic timescales (Large, Herrera, & Velasco, 2015) (see Section 3).

A second key aspect of our canonical oscillator networks is that they can learn and adapt via Hebbian plasticity (Hoppensteadt & Izhikevich, 1996). Equation 2, a Hebbian learning rule, determines the dynamics of plastic connections that alter their amplitude and phase depending on the amplitude and frequency relationship between its source and target (see Section 4).

$$\frac{\tau_i + \tau_j}{2} \dot{c}_{ij} = c_{ij} \left(\lambda_1 + \mu_1 |c_{ij}|^2 + \frac{\epsilon_c \mu_2 |c_{ij}|^4}{1 - \epsilon_c |c_{ij}|^2} \right) + \kappa \frac{z_i}{1 - \sqrt{\epsilon_c} z_i} \cdot \frac{\bar{z}_j}{1 - \sqrt{\epsilon_c} \bar{z}_j} \quad (2)$$

In Eq. 2 c_{ij} is a complex variable representing the amplitude and phase of the plastic connection from the j th oscillator to the i th oscillator. The parameters λ , μ_1 , μ_2 , κ , and ϵ_c determine the dynamics of the plasticity. A simulation of the model defined by Equations 1 and 2 shows that,

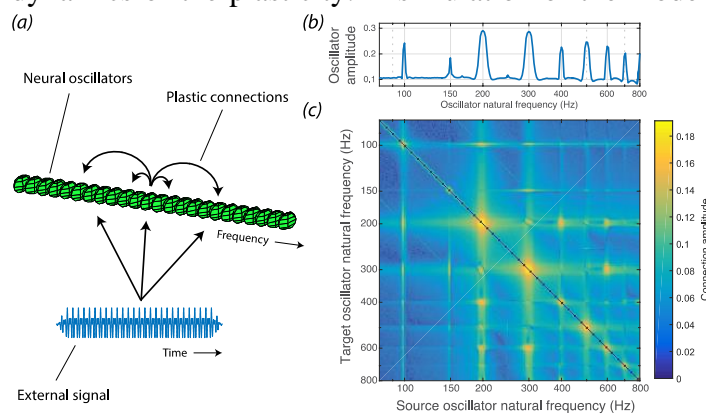


Figure 1.2. A GrFNN model with external forcing and plastic internal connections. (A) Schematic of the model structure. (B) Oscillator amplitudes and (C) plastic connection amplitudes after stimulation with an external signal containing 200 and 300 Hz sinusoids. Note the harmonic structure of the response, including the 100 Hz “missing fundamental”.

of the components (Fig 1.2c shows only amplitude, i.e. “bind” the simultaneous components into an integrated percept.

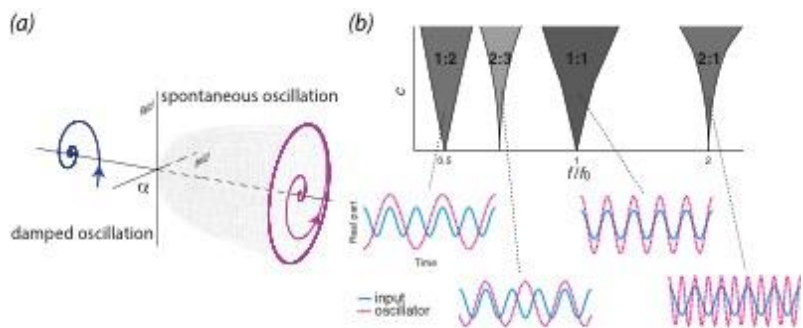


Figure 1.1. (a) Intrinsic oscillatory dynamics can arise through a Hopf bifurcation, where $a = 0$ is the critical point, between damped (left) and spontaneous (right) oscillation. (b) Within each resonance region in the frequency-coupling parameter space (c: coupling strength, f: oscillator intrinsic frequency, f_0 : input frequency) the oscillator mode-locks to the input at the $k:m$ ratio shown. Insets show example inputs and traces produced by the model.

unlike linear filters, canonical oscillators resonate not only to frequencies present in the external signal but also to their harmonics, subharmonics, and nonlinear combinations (Fig 1.2b). Plastic connections grow strong between oscillators if they exhibit certain simple frequency relationships (Fig 1.2c). In the example, a “missing fundamental” stimulus is input to the network (200 ad 300 Hz; Fig 1.2b) as well as other related frequencies. The connection matrix learns amplitude and phase relationships ($|c_{ij}|$) and this information can be used to

Summary: The model described by Equations 1 and 2 is a generic population-level model (Hoppensteadt & Izhikevich, 1997) that captures the fundamental dynamics observed in neuron-level models (Brunel, 2000; Stefanescu & Jirsa, 2008), but is amenable to theoretical and computational analysis (Aronson, Ermentrout, & Kopell, 1990). The model is invariant over temporal and spatial scale, and in Section 5 we use it to model active cochlear resonance to sound (Lerud, Kim, Almonte, Carney, & Large, under revision), brainstem phase-locking to pitch combinations (Lerud, Almonte, Kim, & Large, 2014), and cortical entrainment to rhythmic patterns (e.g., Large et al., 2015). First, however, we describe the theoretical analyses that have enabled us to create such models.

2. Signal Processing by Neural Oscillators

Despite its simple mathematical form, the canonical model for gradient frequency neural networks is still difficult to analyze in its entirety because its dynamics is determined by complex interactions among multiple network components. Oscillators in the network are driven by external forcing and at the same time receive input from other oscillators, and both types of interaction may involve linear and/or nonlinear coupling which can evolve over time via a generalized form of Hebbian plasticity (Large, 2011; Hoppensteadt and Izhikevich, 1996). Our approach is to analyze individual components of the network separately and attempt to understand its overall dynamics as a combination of its component dynamics. To begin, we analyzed and categorized the driven behaviors of canonical oscillators under periodic forcing.

Consider the following differential equation describing an oscillator in the canonical model (or simply, a canonical oscillator) driven by sinusoidal forcing of fixed frequency, ω_0 , and amplitude, F :

$$\dot{z} = z \left(\alpha + i\omega + \beta_1 |z|^2 + \frac{\epsilon \beta_2 |z|^4}{1 - \epsilon |z|^2} \right) + F e^{i\omega_0 t} \quad (3)$$

where $\omega = 2\pi f$ is the radian natural frequency. To understand the response of a gradient frequency network, we focus on how the driven state of an oscillator changes as a function of its natural frequency.

The autonomous behavior of the oscillator (i.e., when $F = 0$) is readily seen when it is brought to polar coordinates using $z = r e^{i\phi}$. Then, the amplitude and phase dynamics are described by

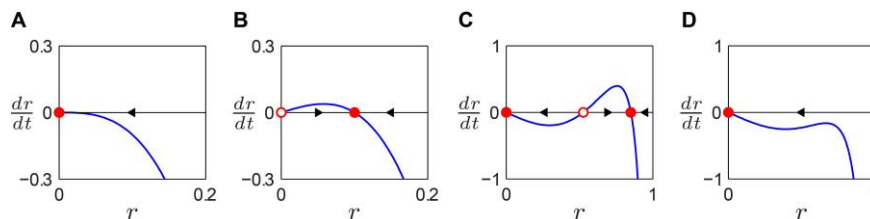


Figure 2.1. Autonomous behavior of a canonical oscillator in different parameter regimes. Amplitude vector field is shown for (A) a critical Hopf regime, (B) a supercritical Hopf regime, (C) a supercritical double limit cycle regime, and (D) a subcritical double limit cycle regime. Filled circles indicate stable fixed points (attractors) and empty circles unstable fixed points (repellers). Arrows indicate the direction of trajectories in the vector field.

arrow indicates (Fig 2.1A). An oscillator with this type of amplitude vector field decays to zero

$$\begin{cases} \dot{r} = \alpha r + \beta_1 r^3 + \frac{\epsilon \beta_2 r^5}{1 - \epsilon r^2} \\ \dot{\phi} = \omega. \end{cases}$$

Depending on the values of α , β_1 , and β_2 , the autonomous amplitude vector field (the first equation above) can have one of four distinct topologies. When \dot{r} decreases monotonically as r increases, the origin is the only fixed point which is stable as the

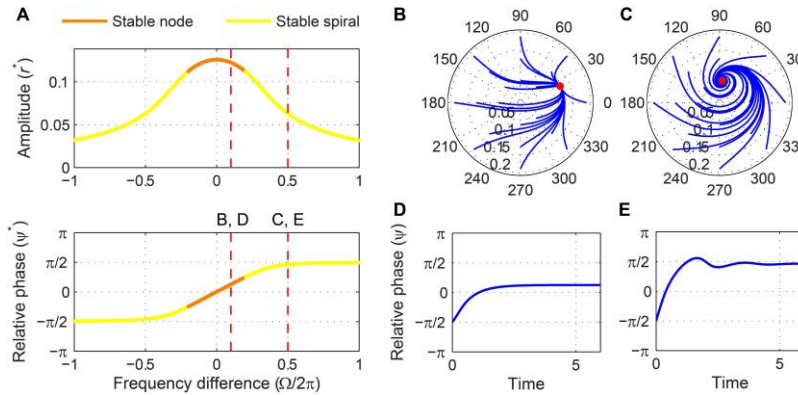


Figure 2.2. Driven behavior of a critical Hopf oscillator. (A) Steady-state amplitude and relative phase as a function of frequency difference ($\alpha = 0$, $\beta_1 = -100$, $\beta_2 = 0$, $F = 0.2$), with vertical dashed lines indicating the frequency differences used for panels B–E, (B) trajectories attracted to a stable node in the (r, ψ) plane starting from a set of different initial conditions ($\Omega/2\pi = 0.1$), (C) trajectories attracted to a stable spiral ($\Omega/2\pi = 0.5$), (D) relative phase plotted over time for a trajectory in panel B (phase locking), and (E) relative phase plotted over time for a trajectory in panel C (phase locking). Filled circles in panels B and C indicate stable fixed points.

When there are three fixed points with two local extrema, two of the fixed points are stable, indicating bistability between equilibrium at zero and spontaneous oscillation at a nonzero amplitude (Fig 2.1C). As the local maximum in the vector field moves below the r axis by, say, decreasing β_1 , the two nonzero fixed points collide and vanish (Fig 2.1D). This transition is called a double limit cycle (hereafter, DLC) bifurcation since it involves two limit cycles (closed orbits) in the (r, ψ) plane, one stable and the other unstable. Thus, we call the regime shown in Fig 2.1C ($\alpha < 0$, $\beta_1 > 0$, $\beta_2 < 0$, local max > 0) *supercritical DLC* and the one shown in Fig 2.1D ($\alpha < 0$, $\beta_1 > 0$, $\beta_2 < 0$, local max < 0) *subcritical DLC*. The subcritical DLC regime has only one stable fixed point at zero but is different from the critical Hopf regime (Fig 2.1A) in that it has a local maximum in the vector field.

To examine how a canonical oscillator responds to external forcing, we bring Equation 3 to polar coordinates, again using $z = re^{i\varphi}$, and express its dynamics in terms of the relative phase $\psi = \varphi - \omega_0 t$ so that a stable fixed point in (r, ψ) indicates a phase-locked state:

$$\begin{cases} \dot{r} = \alpha r + \beta_1 r^3 + \frac{\epsilon \beta_2 r^5}{1 - \epsilon r^2} + F \cos \psi \\ \dot{\psi} = \Omega - \frac{F}{r} \sin \psi, \end{cases} \quad (4)$$

where $\Omega = \omega - \omega_0$ is the frequency difference between the oscillator and the input. We evaluate the stability of fixed point(s) for a range of forcing parameters Ω and F wide enough to encompass all possible qualitatively different driven behaviors of the four regimes of intrinsic parameters introduced above.

while oscillating at its natural frequency. A representative parameter regime for this type is the critical point of a supercritical Hopf bifurcation ($\alpha = 0$, $\beta_1 < 0$). (A subcritical Hopf bifurcation occurs when $\alpha = 0$ and $\beta_1 > 0$.) When \dot{r} increases from the origin and then decreases after a local maximum, there is a stable nonzero fixed point while the origin is rendered unstable (Fig 2.1B). An oscillator of this type shows spontaneous oscillation at the amplitude of the stable fixed point (unless the initial condition is zero). The supercritical branch of a supercritical Hopf bifurcation ($\alpha > 0$, $\beta_1 < 0$) is an example.

2.1 Critical Hopf Oscillators

A stability analysis shows that a critical Hopf oscillator phase-locks to sinusoidal forcing of any frequency and amplitude. For fixed forcing amplitude, the steady-state amplitude r^* is maximum when the forcing frequency is the same as the natural frequency (i.e., $\Omega = 0$), for which the steady-state relative phase ψ^* is zero indicating in-phase synchronization (Fig 2.2A). As the natural frequency and the forcing frequency become more different, r^* decreases monotonically and approaches zero while ψ^* approaches $\pm\frac{\pi}{2}$. While the fixed point (r^*, ψ^*) remains stable for all values of Ω , it changes its stability type from a stable node to a stable spiral as $|\Omega|$ increases from 0. It is clearly seen in the (r, ψ) space that the two attractors have distinct local trajectories (Fig 2.2B and C). The way r and ψ approach their steady-state values in time (monotonic vs. oscillating approach) reflects the difference between a node and a spiral (only the relative phase is shown in Fig 2.2D and E).

2.2 Supercritical Hopf Oscillators

For a supercritical Hopf oscillator under weak forcing, there exist three steady-state solutions for small frequency differences, two of which are a saddle-node pair, and just one unstable solution for large frequency differences (Fig 2.3A). As the frequency difference increases from zero for a fixed forcing amplitude, the saddle and node are lost via a saddle-node invariant-circle (SNIC) bifurcation (also called a saddle-node infinite-period or SNIPER bifurcation), which leaves a stable (attracting) limit-cycle orbit with an unstable fixed point inside (Fig 2.3A–C). For stronger forcing, only one fixed point exists for all values of frequency difference, but it changes from a stable node to a stable spiral then to an unstable spiral as $|\Omega|$ grows from zero (Fig 2.4A). Now the phase-locking boundary is at the transition from a stable spiral to an unstable spiral (i.e., a Hopf bifurcation in the (r, ψ) space).

Outside the phase-locking range for strong forcing, the driven behavior of a supercritical Hopf oscillator can be divided into two categories. Just outside the Hopf boundary, the relative phase changes over time but is bounded and does not traverse the full 2π range (Fig 2.4D), which is called a libration (as opposed to a rotation). When averaged over time, this “phase-trapped” oscillation has the same mean frequency as the input frequency, so it can be described as frequency locking without phase locking (Hoppensteadt and Izhikevich, 1997). As $|\Omega|$ increases further, the relative phase starts making full rotations (Fig 2.4E). At this point, the average

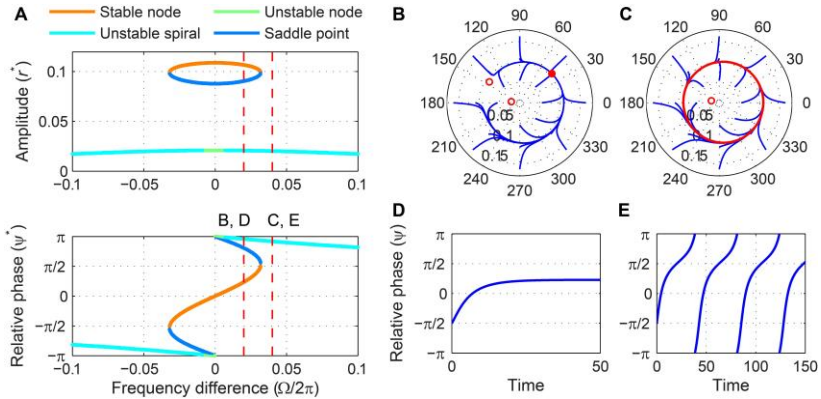


Figure 2.3. Driven behavior of a supercritical Hopf oscillator under weak forcing. (A) Steady-state amplitude and relative phase as a function of frequency difference ($\alpha = 1$, $\beta_1 = -100$, $\beta_2 = 0$, $F = 0.02$), with vertical dashed lines indicating the frequency differences used for panels B–E, (B) trajectories attracted to a stable node in the (r, ψ) plane ($\Omega/2\pi = 0.02$), (C) trajectories drawn to a limit cycle ($\Omega/2\pi = 0.04$), (D) relative phase plotted over time for a trajectory in panel B (phase locking), and (E) relative phase plotted over time for a trajectory in panel C (phase slip). In panels B and C, filled and empty circles indicate stable and unstable fixed points respectively, and red lines show limit-cycle orbits.

instantaneous frequency of the oscillator is different from the input frequency and approaches the natural frequency as $|\Omega|$ approaches infinity. The existence of phase-trapped libration (thus, frequency locking) outside the phase-locking boundary is a distinct feature of the Hopf boundary.

The SNIC phase-locking boundary and the Hopf boundary exist only for weak and strong forcing levels respectively, but the two types of phase-locking boundary coexist for a small range of intermediate forcing level. This region of the forcing parameter space contains a complicated but well-studied set of bifurcations such as the Bogdanov–Takens bifurcation and the cusp point. Also, it is worth noting that the same set of bifurcations are found for other periodically driven nonlinear oscillators or populations of oscillators such as the forced van der Pol oscillator (Holmes & Rand, 1978) and the forced Kuramoto model (Childs & Strogatz, 2008). However, the canonical model analyzed here, with its simple mathematical form, allows closer analytical examination than is possible for more complex models.

2.3 Supercritical Double Limit Cycle Oscillators

In the interest of space, here we will present a summary of the driven behaviors of supercritical DLC oscillators and subcritical DLC oscillators (see Kim & Large, 2015, for a full analysis). These are also summarized in Table 1 and Fig 2.5 below.

When driven by a sinusoid, a supercritical DLC oscillator shows three distinct sets of behaviors depending on the strength of the forcing, and many of these behaviors involve bistability. Under weak forcing, a supercritical DLC oscillator has two stable fixed points for small frequency differences and only one for large frequency differences. The stable fixed point with a small amplitude exists for all values of Ω , but the one with a high amplitude (a stable node) is lost via a SNIC bifurcation and leaves a limit-cycle rotation (phase slip) where it collides with a saddle point. For intermediate forcing amplitudes, the saddle-node pair at high amplitudes still exists for small frequency differences, but the stable fixed point at low amplitudes exists only for large frequency differences. There is a range of intermediate frequency differences for which no stable fixed point exists and all trajectories are attracted to a limit-cycle rotation that the saddle-node pair leaves. As the frequency difference increases, the fixed point inside the limit cycle changes from an unstable node to an unstable spiral and eventually to a stable spiral (i.e. a subcritical Hopf bifurcation). When the forcing amplitude is further increased, only one fixed point exists for any value of frequency difference. The driven state (r, ψ) of a strongly forced supercritical DLC oscillator goes through transitions from a stable node (phase locking), a stable

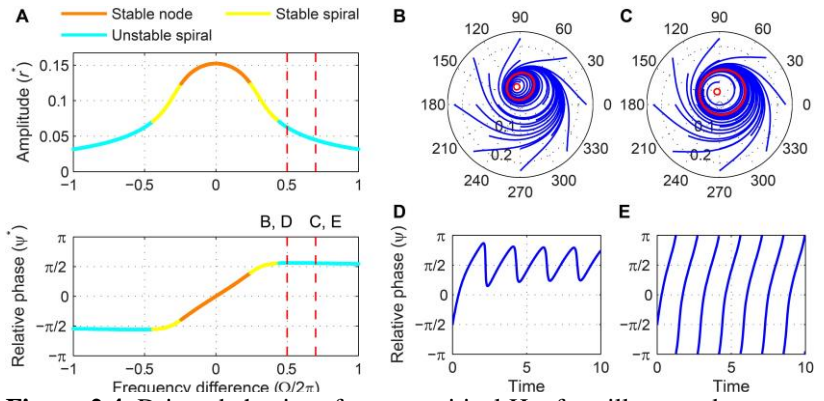


Figure 2.4. Driven behavior of a supercritical Hopf oscillator under strong forcing. (A) Steady-state amplitude and relative phase as a function of frequency difference ($\alpha = 1$, $\beta_1 = -100$, $\beta_2 = 0$, $F = 0.2$), with vertical dashed lines indicating the frequency differences used for panels B–E, (B) trajectories attracted to a phase-trapped libration in the (r, ψ) plane ($\Omega/2\pi = 0.5$), (C) trajectories attracted to a rotation ($\Omega/2\pi = 0.7$), (D) relative phase plotted over time for a trajectory in panel B (phase-trapped frequency locking without phase locking), and (E) relative phase plotted over time for a trajectory in panel C (phase slip). In panels B and C, empty circles indicate unstable fixed points, and red lines show limit-cycle orbits.

spiral (phase locking), a libration around an unstable spiral (frequency locking without phase locking), a rotation around an unstable spiral (phase slip), and lastly bistability between phase locking on a stable spiral and phase slip on a stable limit cycle. So, a strongly forced supercritical DLC oscillator has two phase-locking boundaries, a supercritical Hopf bifurcation and a subcritical Hopf bifurcation.

2.4 Subcritical Double Limit Cycle Oscillators

Like a critical Hopf oscillator, a subcritical DLC oscillator is attracted to an equilibrium at zero when it is not driven. But the presence of a local maximum in the amplitude vector field makes its driven dynamics more varied and interesting than that of a critical Hopf oscillator. Like a supercritical DLC oscillator, a subcritical DLC oscillator exhibits three different sets of driven behaviors depending on the forcing amplitude.

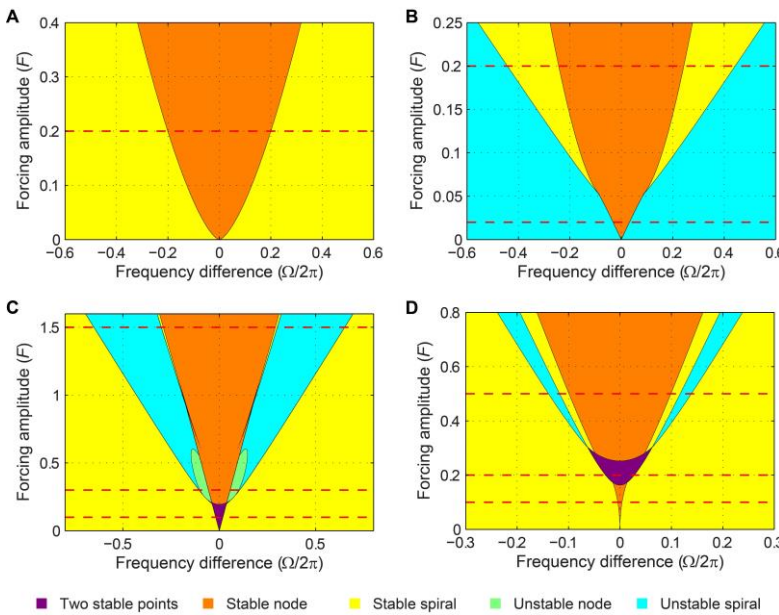


Figure 2.5. Stability regions for a canonical oscillator under sinusoidal forcing. The stability of driven state (r^*, ψ^*) is shown as a function of forcing amplitude and frequency difference for (A) a critical Hopf oscillator ($\alpha = 0, \beta_1 = -100, \beta_2 = 0$), (B) a supercritical Hopf oscillator ($\alpha = 1, \beta_1 = -100, \beta_2 = 0$), (C) a supercritical double limit cycle oscillator ($\alpha = -1, \beta_1 = 4, \beta_2 = -1, \varepsilon = 1$), and (D) a subcritical double limit cycle oscillator ($\alpha = -1, \beta_1 = 2.5, \beta_2 = -1, \varepsilon = 1$). The color indicates the stability type of a stable fixed point if there is one (purple if there are two). If there is no stable fixed point, the color indicates the stability of an unstable fixed point. Dashed horizontal lines indicate the forcing amplitudes used for Figs. 2.2–2.4.

the limit cycle does not grow into a rotation that encompasses the origin, which is the case for a supercritical DLC oscillator. Instead, it shrinks back and turns into a stable spiral via another supercritical Hopf bifurcation. In the absence of a SNIC or subcritical Hopf bifurcation, a strongly driven subcritical DLC oscillator shows no bistability and, since the only non-locked behavior is a libration, it either phase-locks or frequency-locks to the input for all values of Ω .

2.5 Classification of Parameter Regimes by Driven Behavior

We can classify all possible parameter settings for canonical oscillators into four regimes with distinct driven behaviors (Table 1 and Fig. 2.5). Oscillators with an autonomous amplitude

For weak forcing, it behaves like a critical Hopf oscillator, with its driven state attracted to a stable node when $|\Omega|$ is small and to a stable spiral when $|\Omega|$ is large. For intermediate forcing amplitudes, a pair of fixed points appears at high amplitudes and they are lost via a saddle-node bifurcation at a certain frequency difference, but this saddle-node bifurcation does not leave a limit cycle like a SNIC bifurcation. When driven strongly, a subcritical DLC oscillator has the same set of fixed points as a supercritical DLC oscillator—a stable node, a stable spiral, an unstable spiral, and a stable spiral as $|\Omega|$ increases from zero. A supercritical Hopf bifurcation occurs at the first phase-locking boundary, where a stable spiral turns unstable and a stable limit cycle grows around it. However,

vector field that monotonically decreases from zero with no local extremum (Fig 2.1A) have the same set of driven behaviors as a critical Hopf oscillator ($\alpha = 0, \beta_1 < 0, \beta_2 = 0$). Linear oscillators ($\alpha < 0, \beta_1 = 0, \beta_2 = 0$) belong to this category. Oscillators whose amplitude vector fields have one local maximum (Fig 2.1B) have the same set of driven behaviors and bifurcations as a supercritical Hopf oscillator ($\alpha > 0, \beta_1 < 0, \beta_2 = 0$). Oscillators with $\alpha < 0, \beta_1 > 0$, and $\beta_2 < 0$ are divided into three groups depending on whether the local maximum of the amplitude vector field is above zero (Fig 2.1C, a supercritical DLC oscillator), is below zero (Fig 2.1D, a subcritical DLC oscillator), or does not exist (with the same driven behaviors as a critical Hopf oscillator).

Table 1. Classification of parameter regimes by driven behavior

α	β_1	β_2	Local extremum ^a	Discussed as	Bifurcations ^b
–	0	0	None		None
0	–	0		Critical Hopf	
0	0	–			
–	–	0			
–	0	–			
0	–	–			
–	–	–			
–	+	–	(No max)		
+	–	0	One	Supercritical Hopf	SNIC (low F); Super-Hopf (high F)
+	0	–			
0	+	–			
+	–	–			
+	+	–			
–	+	–	Two (max > 0)	Supercritical DLC	SNIC (low F); SNIC, Sub-Hopf (mid F); Super-Hopf, Sub-Hopf (high F)
–	+	–	Two (max < 0)	Subcritical DLC	None (low F); SN (mid F); Super-Hopf, Super-Hopf (high F)

SNIC, saddle-node bifurcation on an invariant circle; Super-Hopf, supercritical Hopf bifurcation; Sub-Hopf, subcritical Hopf bifurcation; SN, saddle-node bifurcation.

^aThe number of local extrema in the autonomous amplitude vector field.

^bBifurcations at phase-locking boundaries.

3. Pattern Formation, Analysis and Recognition

As shown in Section 1, we use dynamic patterns of multi-frequency oscillations formed in gradient frequency neural networks to explain and model auditory neural processing and auditory perception. Here we present the results of a series of analysis for systems of coupled oscillators which were done to better understand and utilize the complex network dynamics of GrFNs.

3.1 Stability Analysis of Coupled Oscillators: Phase-Locking

Here we analyze the following system of two canonical oscillators coupled to each other:

$$\begin{cases} \dot{z}_1 = z_1 \left(\alpha + i\omega_1 + \beta_1 |z_1|^2 + \frac{\epsilon \beta_2 |z_1|^4}{1 - \epsilon |z_1|^2} \right) + cz_2 \\ \dot{z}_2 = z_2 \left(\alpha + i\omega_2 + \beta_1 |z_2|^2 + \frac{\epsilon \beta_2 |z_2|^4}{1 - \epsilon |z_2|^2} \right) + cz_1 \end{cases} \quad (5)$$

whose polar form is

$$\begin{cases} \dot{r}_1 = \alpha r_1 + \beta_1 r_1^3 + \frac{\epsilon \beta_2 r_1^5}{1-\epsilon r_1^2} + cr_2 \cos \psi \\ \dot{r}_2 = \alpha r_2 + \beta_1 r_2^3 + \frac{\epsilon \beta_2 r_2^5}{1-\epsilon r_2^2} + cr_1 \cos \psi \\ \dot{\psi} = \Omega - \frac{c(r_1^2 + r_2^2)}{r_1 r_2} \sin \psi. \end{cases} \quad (6)$$

where $z_i = r_i e^{i\varphi_i}$, $\psi = \varphi_1 - \varphi_2$ and $\Omega = \omega_1 - \omega_2$. We present the analysis of two coupled oscillators for each parameter regime identified in Section 2.

Critical Hopf oscillators ($\alpha = 0, \beta_1 < 0, \beta_2 = 0$). Eliminating $\cos \psi^*$ from the steady-state amplitude equations reveals that there are only fixed points with symmetric amplitudes (i.e. $r_1^* = r_2^*$). Then, we can reduce Eq. 6 to a two-dimensional system with the phase equation independent of amplitude ($r \equiv r_1 = r_2$):

$$\begin{cases} \dot{r} = \beta_1 r^3 + cr \cos \psi \\ \dot{\psi} = \Omega - 2c \sin \psi. \end{cases}$$

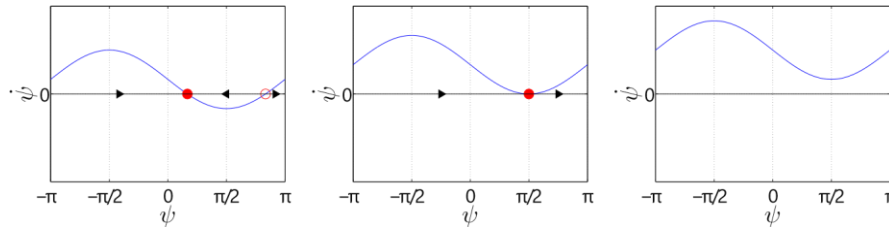


Figure 3.1. Vector field of the relative phase of two coupled oscillator with symmetric amplitudes when $0 < \Omega < 2c$ (left), $\Omega = 2c$ (middle), and $\Omega > 2c$ (right).

no ψ^* (i.e. no phase-locking) and ψ rotates in either positive or negative direction. Note that ψ changes slowly (a “bottleneck”) near $\psi = \frac{\pi}{2}$ when $\Omega > 2c$ and near $\psi = -\frac{\pi}{2}$ when $\Omega < -2c$.

The steady-state solution of the amplitude equation shows that nonzero steady-state amplitude exists for $|\Omega| < 2c$ and it drops to zero at the boundary (Fig. 3.2). The Jacobian matrix and its trace and determinant suggest that the fixed point always lies on the border between stable nodes and stable spirals (it is a star node with both eigenvalues at $-2c$). Zero solution $r_1^* = r_2^* = 0$ is also a possibility for coupled critical oscillators, regardless of $|\Omega|$ being greater or smaller than $2c$. A perturbation analysis shows that the zero solution is unstable for $|\Omega| < 2c$, and stable for $|\Omega| \geq 2c$.

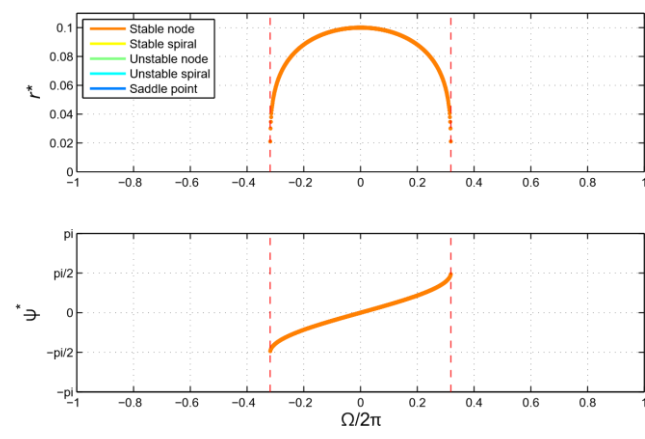


Figure 3.2. Steady-state amplitude and relative phase of two coupled critical Hopf oscillators ($\alpha = 0, \beta_1 = -100, c = 1$). Though the fixed points are colored orange, they are all star nodes.

The steady-state solution of the phase equation above indicates that there is a phase-locking boundary at $|\Omega| = 2c$. There is a node-saddle pair when $|\Omega| < 2c$, which vanishes at the boundary (Fig. 3.1).

When $|\Omega| > 2c$, there is no ψ^* (i.e. no phase-locking) and ψ rotates in either positive or negative direction. Note that ψ changes slowly (a “bottleneck”) near $\psi = \frac{\pi}{2}$ when $\Omega > 2c$ and near $\psi = -\frac{\pi}{2}$ when $\Omega < -2c$.

The steady-state solution of the amplitude equation shows that nonzero steady-state amplitude exists for $|\Omega| < 2c$ and it drops to zero at the boundary (Fig. 3.2). The Jacobian matrix and its trace and determinant suggest that the fixed point always lies on the border between stable nodes and stable spirals (it is a star node with both eigenvalues at $-2c$). Zero solution $r_1^* = r_2^* = 0$ is also a possibility for coupled critical oscillators, regardless of $|\Omega|$ being greater or smaller than $2c$. A perturbation analysis shows that the zero solution is unstable for $|\Omega| < 2c$, and stable for $|\Omega| \geq 2c$.

Supercritical Hopf oscillators ($\alpha > 0, \beta_1 < 0, \beta_2 = 0$). These are two possible solutions for two coupled supercritical oscillators: solutions with symmetric

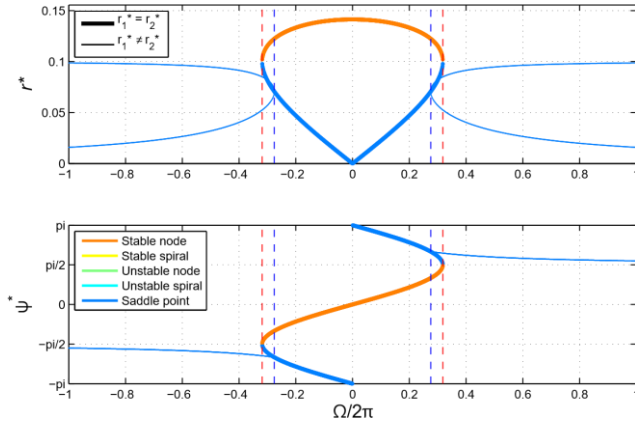


Figure 3.3. Steady-state amplitudes (both symmetric and asymmetric) and relative phase of two coupled supercritical Hopf oscillators ($\alpha = 1$, $\beta_1 = -100$, $c = 1$). The thick lines indicate fixed points with symmetric amplitudes and the thin lines those with asymmetric amplitudes.

However, an examination of the Jacobian matrix reveals that asymmetric solutions are all saddle points. So, the only stable solutions are coupled supercritical Hopf oscillators are symmetric solutions (Fig. 3.3).

Supercritical DLC oscillators ($\alpha < 0$, $\beta_1 > 0$, $\beta_2 < 0$, local max > 0). Fig. 3.4 shows the stability of fixed points for supercritical DLC oscillators with two different levels of coupling strength. Symmetric solutions (thick lines) exist only when $|\Omega| \leq 2c$. Within this range, there is only one stable nonzero fixed point with symmetric amplitudes, which is always a node. They also have stable fixed points with asymmetric amplitudes, due to their bistability. When coupling is weak enough, stable asymmetric solutions exist for all values of Ω . For stronger coupling, they exist for large values of $|\Omega|$ only. Three distinct behaviors are possible for $|\Omega| > 2c$. Zero solution is stable so that both oscillators can decay to zero if initial amplitudes are small. When both initial amplitudes are big enough, oscillators can stay not locked to each other, with relative phase ψ rotating. If one oscillator starts from small initial amplitude and the other from big amplitude, they could phase-lock with asymmetric steady-state amplitudes.

Subcritical DLC oscillators ($\alpha < 0$, $\beta_1 > 0$, $\beta_2 < 0$, local max < 0). Subcritical DLC

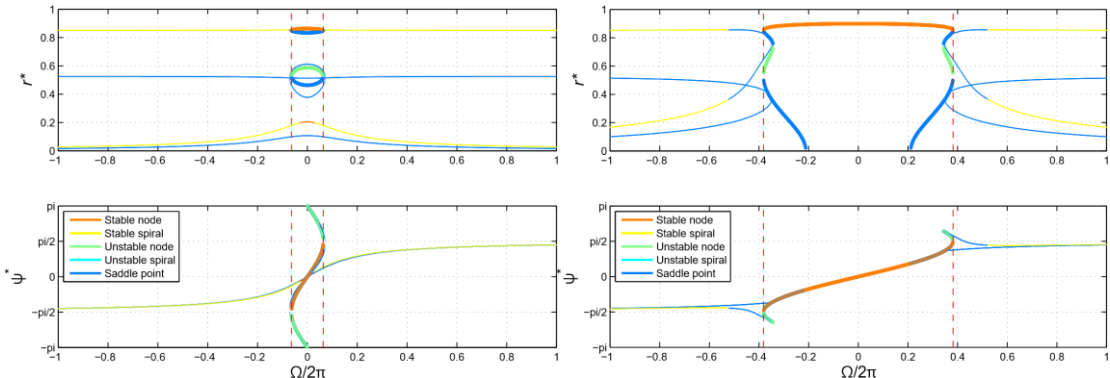


Figure 3.4. Steady-state amplitude and relative phase of two coupled supercritical DLC oscillators ($\alpha = -1$, $\beta_1 = 4$, $\beta_2 = -1$) with weak coupling ($c = 0.2$, left) and strong coupling ($c = 1.2$, right). Thick lines represent symmetric solutions and thin lines asymmetric ones. The dashed lines indicate the phase-locking boundary for symmetric behaviors $|\Omega| = 2c$.

amplitudes and those with asymmetric amplitudes. The symmetric solution is

$$r^* = \sqrt{\frac{\alpha \pm \sqrt{c^2 - \frac{\Omega^2}{4}}}{\beta_1}}.$$

Examination of the Jacobian matrix indicates the first solution (the bigger r^*) is always a stable node and the second one, if it exists, is a saddle point. The stable node is lost via a saddle-node bifurcation at the locking boundary, which is predictable from the observation that the relative phase rotates right outside the boundary (Fig. 3.3, bold lines). The asymmetric solutions are

$$r_1^* = \sqrt{-\frac{\alpha}{2\beta_1} \left(1 \pm \sqrt{1 - \frac{4c^2}{\alpha^2 + \Omega^2}} \right)}$$

and the other amplitude is obtained by

$$r_1^{*2} + r_2^{*2} = -\frac{\alpha}{\beta_1}.$$

oscillators have nonzero symmetric r^* 's for a subset of $|\Omega| \leq 2c$. When coupling is weak and satisfies the following condition, there is no nonzero r^* for all values of Ω and zero solution is the only stable fixed point:

$$c^2 < \left(\frac{2\beta_2 - \beta_1 + 2\sqrt{\beta_2(\beta_2 - \beta_1)}}{\epsilon} - \alpha \right)^2.$$

This is when the local maximum in amplitude vector field is below zero even for $\Omega = 0$. With stronger coupling, nonzero symmetric r^* 's exist for the following range of Ω , which is a subset of $|\Omega| \leq 2c$:

$$|\Omega| < 2\sqrt{c^2 - \left(\frac{2\beta_2 - \beta_1 + 2\sqrt{\beta_2(\beta_2 - \beta_1)}}{\epsilon} - \alpha \right)^2}.$$

As shown in Fig. 3.5, fixed points with asymmetric amplitudes exist for coupled subcritical DLC oscillators. Most of them are unstable saddle points, but with strong coupling there is a narrow range of $|\Omega|$ just outside $|\Omega| = 2c$ where stable spirals exist.

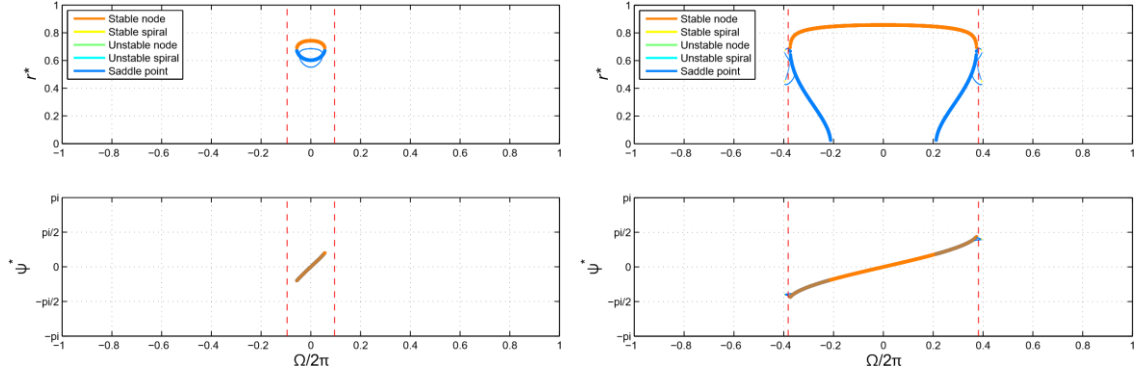


Figure 3.5. Steady-state amplitude and relative phase of two coupled subcritical DLC oscillators ($\alpha = -1$, $\beta_1 = 2.5$, $\beta_2 = -1$) with weak coupling ($c = 0.3$, left) and strong coupling ($c = 1.2$, right).

3.2 Stability Analysis of Coupled Oscillators: Mode-Locking

When two oscillators have natural frequencies whose ratio is close to an integer ratio, they can mode-lock to each other via resonant monomials. Two canonical oscillators mode-locking to each other can be described by

$$\begin{cases} \dot{z}_1 = z_1 \left(\alpha + i\omega_1 + \beta_1 |z_1|^2 + \frac{\epsilon \beta_2 |z_1|^4}{1 - \epsilon |z_1|^2} \right) + \epsilon \frac{k+m-2}{2} c z_2^k \bar{z}_1^{m-1} \\ \dot{z}_2 = z_2 \left(\alpha + i\omega_2 + \beta_1 |z_2|^2 + \frac{\epsilon \beta_2 |z_2|^4}{1 - \epsilon |z_2|^2} \right) + \epsilon \frac{k+m-2}{2} c z_1^m \bar{z}_2^{k-1} \end{cases},$$

for which we assume $\beta_2 < 0$ in order to make the system stable given arbitrarily high k and m . We bring the system to polar coordinates using $z_i = r_i e^{i\varphi_i}$ and define $\psi = m\varphi_1 - k\varphi_2$ and $\Omega = m\omega_1 - k\omega_2$ to get

$$\begin{cases} \dot{r}_1 = \alpha r_1 + \beta_1 r_1^3 + \frac{\epsilon \beta_2 r_1^5}{1 - \epsilon r_1^2} + \epsilon \frac{k+m-2}{2} c r_2^k r_1^{m-1} \cos \psi \\ \dot{r}_2 = \alpha r_2 + \beta_1 r_2^3 + \frac{\epsilon \beta_2 r_2^5}{1 - \epsilon r_2^2} + \epsilon \frac{k+m-2}{2} c r_1^m r_2^{k-1} \cos \psi \\ \dot{\psi} = \Omega - \epsilon \frac{k+m-2}{2} c r_1^{m-2} r_2^{k-2} (k r_1^2 + m r_2^2) \sin \psi. \end{cases}$$

Assuming symmetric solutions, the system can be a two-dimensional system of r ($\equiv r_1 = r_2$) and ψ , for which the steady-state solutions can be obtained by solving

$$\left(\alpha + \beta_1 r^{*2} + \frac{\epsilon \beta_2 r^{*4}}{1 - \epsilon r^{*2}}\right)^2 + \left(\frac{\Omega}{k+m}\right)^2 = e^{k+m-2} c^2 r^{*2(k+m-2)}$$

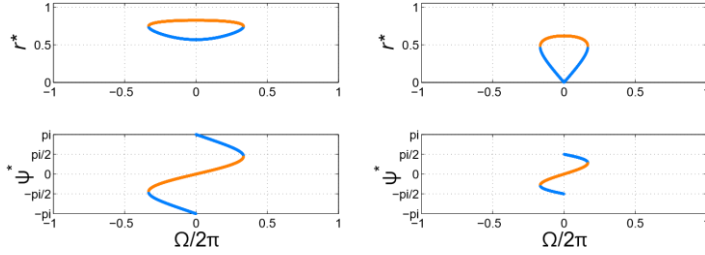


Figure 3.6. Steady-state amplitude and relative phase of two oscillators coupled via resonant monomials for 2:1 mode-locking: supercritical Hopf oscillators ($\alpha = 1, \beta_1 = -1, \beta_2 = -1, \epsilon = 0.9, c = 1$, left) and critical Hopf oscillators ($\alpha = 0, \beta_1 = -1, \beta_2 = -1, \epsilon = 0.9, c = 1$, right).

supercritical Hopf oscillators and critical Hopf oscillators have only symmetric solutions. For both, stability is lost through a saddle-node bifurcation. Supercritical DLC oscillators have both symmetric and asymmetric stable solutions (Fig. 3.7, left). Note that for asymmetric solutions, which are stable spirals, r_2^* is bigger than r_1^* . There is no asymmetric solution with $r_1^* > r_2^*$. This is because the system is asymmetric with respect to r_1 and r_2 due to unequal $k = 2$ and $m = 1$.

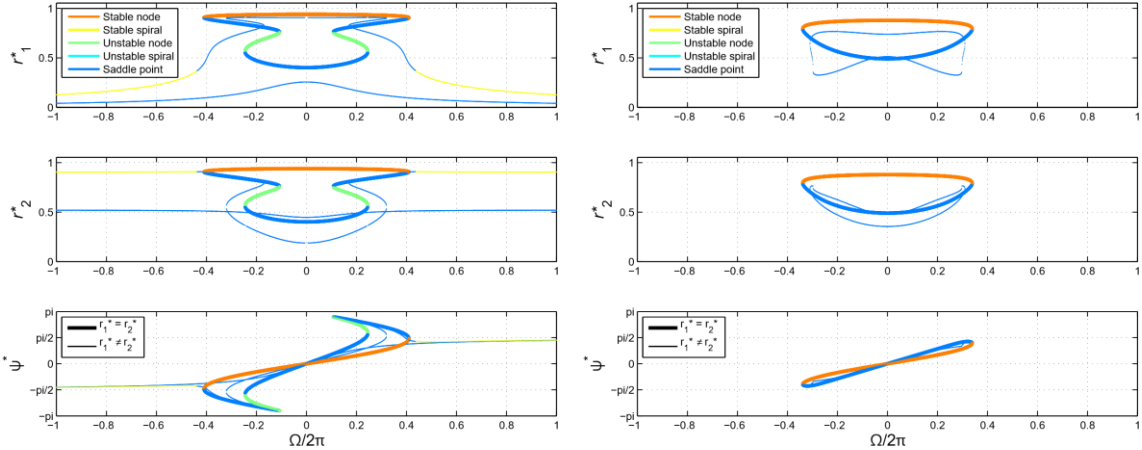


Figure 3.7. Steady-state amplitude and relative phase of two supercritical DLC oscillators ($\alpha = -1, \beta_1 = 4, \beta_2 = -1, \epsilon = 0.9, c = 1$, left) and two subcritical DLC oscillators ($\alpha = -1, \beta_1 = 2.5, \beta_2 = -1, \epsilon = 0.9, c = 1$, right), each coupled via resonant monomials for 2:1 mode-locking.

Subcritical DLC oscillators also have both symmetric and asymmetric solutions, but only a half of symmetric solutions are stable (Fig. 3.7, right).

4. Hebbian Learning and Scene Analysis

Hoppensteadt and Izhikevich (1996, 1997) showed that a weakly connected network of neural oscillators of identical natural frequencies can memorize phase differences between them if synaptic connections change in time according to complex Hebbian learning rule:

$$\begin{cases} z'_i = (\rho_i + i\omega) z_i - z_i |z_i|^2 + \sum_{j=1}^n c_{ij} z_j, & i = 1, \dots, n \\ c'_{ij} = -\gamma c_{ij} + k_{ij} z_i \bar{z}_j, & i \neq j \end{cases}$$

To obtain asymmetric solutions, we must go back to the original three-dimensional system. We do not present the details of the procedure since equations involved in getting asymmetric solutions are too complicated to list here. Since mode-locking dynamics do not change qualitatively for different k 's and m 's, a general overview of both symmetric and asymmetric behaviors is presented below for $k = 2, m = 1$ only.

As shown in Fig. 3.6, both

where $' = d/d\tau$, $\tau = \varepsilon t$ is ‘slow’ time, and γ and k_{ij} are positive real numbers. Note that the learning rule has only a linear intrinsic term and an input term. When z_i and z_j oscillate at the same frequency, the input term $k_{ij}z_i\bar{z}_j$ becomes a complex constant whose phase is the phase difference between z_i and z_j . So, the phase of c_{ij} eventually comes to match the phase difference between the oscillators it connects.

We expanded Hoppensteadt and Izhikevich’s single-frequency network with linear learning rule into a multi-frequency network with nonlinear learning rule. We show that this expansion gives rise to a set of rich dynamics that are not observed in either single-frequency systems or systems without plasticity. Here, we analyze the dynamics of two simplest oscillator systems with plastic connections: an oscillator with plastic coupling to single external input and two oscillators connected by plastic coupling.

4.1 Plastic Coupling to External Forcing

Consider a single oscillator z that is driven by external forcing x via plastic coupling c . Introducing fully expanded intrinsic terms to both the oscillator equation and the learning rule gives us the following system:

$$\begin{cases} \dot{z} = z \left(\alpha + i\omega + \beta_1 |z|^2 + \frac{\epsilon\beta_2 |z|^4}{1-\epsilon|z|^2} \right) + cx \\ \dot{c} = c \left(\lambda + \mu_1 |c|^2 + \frac{\epsilon_c \mu_2 |c|^4}{1-\epsilon_c |c|^2} \right) + \kappa z \bar{x} \end{cases}$$

where κ is a positive real number representing learning rate.

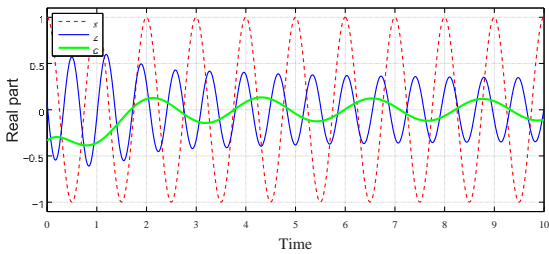


Figure 4.1. Waveform of sinusoidal forcing x , a critical Hopf oscillator z , and plastic coupling c .

frequency and, given this frequency is not too far from zero, we can expect that c would phase-lock to this oscillating input and oscillate at the difference frequency (Fig. 4.1).

To carry out the analysis further, we transform the system to polar coordinates. Assuming sinusoidal forcing of constant amplitude and frequency ($x = Fe^{i\vartheta}$, $\dot{\vartheta} = \omega_0$) and defining $z = re^{i\varphi}$ and $c = Ae^{i\theta}$, it becomes

$$\begin{cases} \dot{r} = \alpha r + \beta_1 r^3 + \frac{\epsilon\beta_2 r^5}{1-\epsilon r^2} + FA \cos(\theta + \vartheta - \phi) \\ \dot{\phi} = \omega + \frac{FA}{r} \sin(\theta + \vartheta - \phi) \\ \dot{A} = \lambda A + \mu_1 A^3 + \frac{\epsilon_c \mu_2 A^5}{1-\epsilon_c A^2} + \kappa Fr \cos(\phi - \vartheta - \theta) \\ \dot{\theta} = \frac{\kappa Fr}{A} \sin(\phi - \vartheta - \theta). \end{cases}$$

Since the only angle that appears on the right-hand side of the above equations is $\theta + \vartheta - \phi$, we define it as ψ and get the following three-dimensional system:

$$\begin{cases} \dot{r} = \alpha r + \beta_1 r^3 + \frac{\epsilon\beta_2 r^5}{1-\epsilon r^2} + FA \cos \psi \\ \dot{A} = \lambda A + \mu_1 A^3 + \frac{\epsilon_c \mu_2 A^5}{1-\epsilon_c A^2} + \kappa Fr \cos \psi \\ \dot{\psi} = -\Omega - \frac{F(\kappa r^2 + A^2)}{rA} \sin \psi \end{cases}$$

From the form of the learning rule, we can treat the connection c as an oscillator whose natural frequency is zero. (Note that there is no imaginary number like $i\omega$ in the intrinsic part of the equation.) This means that c resonates maximally when its input $\kappa z \bar{x}$ has constant phase, which happens when z and x oscillate at the same frequency. When z and x are not oscillating at the same frequency, on the other hand, c is driven by an input that oscillates at the difference frequency.

When z and x are not oscillating at the same frequency, on the other hand, c is driven by an input that oscillates at the difference frequency.

where $\Omega = \omega - \omega_0$. Since the fully expanded system is difficult, if not impossible, to solve, let us examine the following truncated version (i.e. we assume $\beta_2 = \mu_2 = 0$):

$$\begin{cases} \dot{r} = \alpha r + \beta_1 r^3 + FA \cos \psi \\ \dot{A} = \lambda A + \mu_1 A^3 + \kappa Fr \cos \psi \\ \dot{\psi} = -\Omega - \frac{F(\kappa r^2 + A^2)}{rA} \sin \psi. \end{cases}$$

Now that both the oscillator and the learning rule have multiple parameter regimes with distinct behaviors, we are going to briefly describe each combination of the regimes for oscillator and learning rule. First, let us examine the system consisting of a critical Hopf oscillator and linear learning rule—we call it a critical-linear system. Fig. 4.2 shows r^* , A^* , ψ^* and steady-state $\dot{\theta}$ of a critical-linear system as functions of Ω . The critical-linear system has a stable fixed point for all values of Ω , a stable node for small $|\Omega|$ and a stable spiral for large $|\Omega|$. Notice that the oscillator's instantaneous frequency is slower than its natural frequency when the oscillator's natural frequency is greater than the input frequency, and the other way around when the natural frequency is smaller than the input frequency. See also that the connection's instantaneous frequency, $\dot{\theta}$, is always between zero and Ω (marked by the red dashed line). Since $\dot{\theta} = \dot{\phi} - \omega_0$ when the system is in a steady state, this indicates that $\dot{\phi}$ is always between ω and ω_0 . We also observe in Fig. 4.2 that as $|\Omega|$ increases, $\dot{\theta}$ approaches Ω and hence $\dot{\phi}$ approaches ω . So,

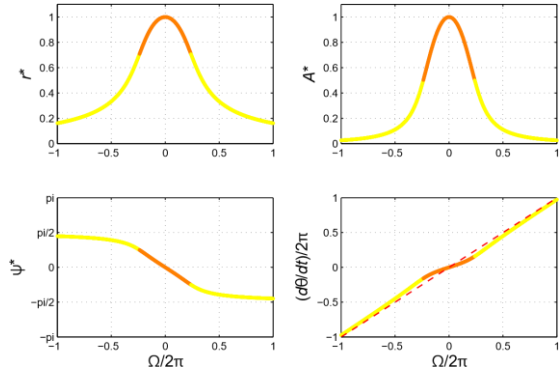


Figure 4.2. Steady-state solutions and their stability for a critical-linear driven system ($\alpha = 0$, $\beta_1 = -1$, $\beta_2 = 0$, $\varepsilon = 0$, $\lambda = -1$, $\mu_1 = 0$, $\mu_2 = 0$, $\varepsilon_c = 0$, $\kappa = 1$, $F = 1$).

when $|\Omega|$ is large, z oscillates near its natural frequency while c oscillates with small amplitude to cope with the big difference between z 's instantaneous frequency and the input frequency.

For a critical-critical system, stable fixed points exist only for small values of $|\Omega|$ and they appear to lie on the border between stable nodes and stable spirals. Outside the locking range, both the oscillator and the connection slowly decay to zero with their amplitude fluctuating. The critical-supercritical system shown in Fig. 4.3 exhibits interesting dynamics.

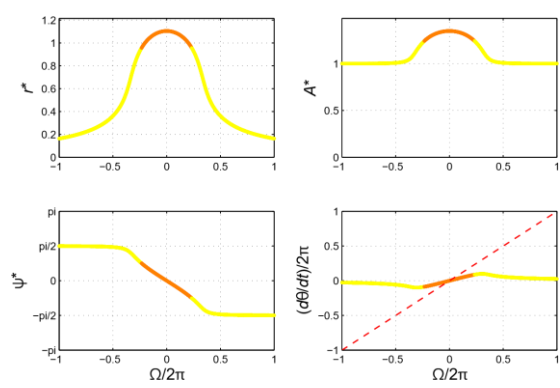


Figure 4.3. Steady-state solutions and their stability for a critical-supercritical driven system ($\alpha = 0$, $\beta_1 = -1$, $\beta_2 = 0$, $\varepsilon = 0$, $\lambda = 1$, $\mu_1 = -1$, $\mu_2 = 0$, $\varepsilon_c = 0$, $\kappa = 1$, $F = 1$).

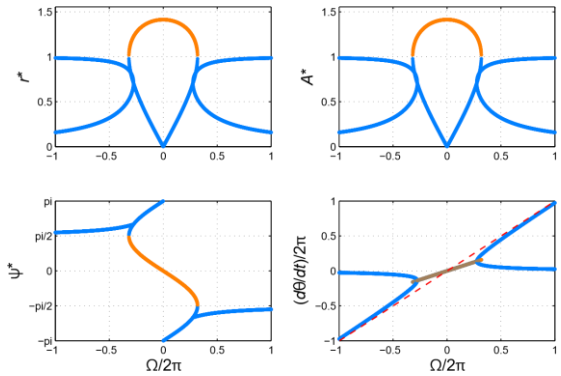


Figure 4.4. Steady-state solutions and their stability for a supercritical-supercritical driven system ($\alpha = 1$, $\beta_1 = -1$, $\beta_2 = 0$, $\varepsilon = 0$, $\lambda = 1$, $\mu_1 = -1$, $\mu_2 = 0$, $\varepsilon_c = 0$, $\kappa = 1$, $F = 1$).

Contrary to the critical-linear system shown earlier, $\dot{\theta}$ converges to zero (thus $\dot{\phi}$ approaches ω_0) as $|\Omega|$ increases toward infinity. This is because the connection has nonzero spontaneous amplitude so that its amplitude cannot be lowered indefinitely. The supercritical-linear and supercritical-critical systems have similar overall dynamics to the critical-linear system, except that the oscillators' amplitude converges to their nonzero spontaneous amplitude as $|\Omega|$ increases. The supercritical-supercritical system shown in Fig. 4.4 has stable fixed points for only small $|\Omega|$ and the locking boundary is a saddle-node bifurcation point. Outside the locking range, both the oscillator and the connection fluctuate near their spontaneous amplitudes and intrinsic frequencies.

4.2 Two Oscillators with Plastic Coupling

The dynamics of two canonical oscillators connected through plastic coupling can be described by

$$\begin{cases} \dot{z}_1 = z_1 \left(\alpha + i\omega_1 + \beta_1 |z_1|^2 + \frac{\epsilon \beta_2 |z_1|^4}{1 - \epsilon |z_1|^2} \right) + c_{12} z_2 \\ \dot{z}_2 = z_2 \left(\alpha + i\omega_2 + \beta_1 |z_2|^2 + \frac{\epsilon \beta_2 |z_2|^4}{1 - \epsilon |z_2|^2} \right) + c_{21} z_1 \\ \dot{c}_{12} = c_{12} \left(\lambda + \mu_1 |c_{12}|^2 + \frac{\epsilon_c \mu_2 |c_{12}|^4}{1 - \epsilon_c |c_{12}|^2} \right) + \kappa z_1 \bar{z}_2 \\ \dot{c}_{21} = c_{21} \left(\lambda + \mu_1 |c_{21}|^2 + \frac{\epsilon_c \mu_2 |c_{21}|^4}{1 - \epsilon_c |c_{21}|^2} \right) + \kappa z_2 \bar{z}_1. \end{cases}$$

Defining $z_i = r_i e^{i\theta_i}$ and $c_{ij} = A_{ij} e^{i\theta_{ij}}$, the above system is transformed to

$$\begin{cases} \dot{r}_1 = \alpha r_1 + \beta_1 r_1^3 + \frac{\epsilon \beta_2 r_1^5}{1 - \epsilon r_1^2} + A_{12} r_2 \cos(\theta_{12} + \phi_2 - \phi_1) \\ \dot{\phi}_1 = \omega_1 + \frac{A_{12} r_2}{r_1} \sin(\theta_{12} + \phi_2 - \phi_1) \\ \dot{r}_2 = \alpha r_2 + \beta_1 r_2^3 + \frac{\epsilon \beta_2 r_2^5}{1 - \epsilon r_2^2} + A_{21} r_1 \cos(\theta_{21} + \phi_1 - \phi_2) \\ \dot{\phi}_2 = \omega_2 + \frac{A_{21} r_1}{r_2} \sin(\theta_{21} + \phi_1 - \phi_2) \\ \dot{A}_{12} = \lambda A_{12} + \mu_1 A_{12}^3 + \frac{\epsilon_c \mu_2 A_{12}^5}{1 - \epsilon_c A_{12}^2} + \kappa r_1 r_2 \cos(\phi_1 - \phi_2 - \theta_{12}) \\ \dot{\theta}_{12} = \frac{\kappa r_1 r_2}{A_{12}} \sin(\phi_1 - \phi_2 - \theta_{12}) \\ \dot{A}_{21} = \lambda A_{21} + \mu_1 A_{21}^3 + \frac{\epsilon_c \mu_2 A_{21}^5}{1 - \epsilon_c A_{21}^2} + \kappa r_2 r_1 \cos(\phi_2 - \phi_1 - \theta_{21}) \\ \dot{\theta}_{21} = \frac{\kappa r_2 r_1}{A_{21}} \sin(\phi_2 - \phi_1 - \theta_{21}). \end{cases}$$

Note that there are only two distinct arguments for trigonometric functions on the right-hand side of the equations above. Defining them as $\psi_{12} = \theta_{12} - \phi_1 + \phi_2$ and $\psi_{21} = \theta_{21} - \phi_2 + \phi_1$ turns the above eight-dimensional system into a six-dimensional one:

$$\begin{cases} \dot{r}_1 = \alpha r_1 + \beta_1 r_1^3 + \frac{\epsilon \beta_2 r_1^5}{1 - \epsilon r_1^2} + A_{12} r_2 \cos \psi_{12} \\ \dot{r}_2 = \alpha r_2 + \beta_1 r_2^3 + \frac{\epsilon \beta_2 r_2^5}{1 - \epsilon r_2^2} + A_{21} r_1 \cos \psi_{21} \\ \dot{A}_{12} = \lambda A_{12} + \mu_1 A_{12}^3 + \frac{\epsilon_c \mu_2 A_{12}^5}{1 - \epsilon_c A_{12}^2} + \kappa r_1 r_2 \cos \psi_{12} \\ \dot{A}_{21} = \lambda A_{21} + \mu_1 A_{21}^3 + \frac{\epsilon_c \mu_2 A_{21}^5}{1 - \epsilon_c A_{21}^2} + \kappa r_2 r_1 \cos \psi_{21} \\ \dot{\psi}_{12} = -\Omega - \frac{r_2 (\kappa r_1^2 + A_{12}^2)}{r_1 A_{12}} \sin \psi_{12} + \frac{A_{21} r_1}{r_2} \sin \psi_{21} \\ \dot{\psi}_{21} = \Omega - \frac{r_1 (\kappa r_2^2 + A_{21}^2)}{r_2 A_{21}} \sin \psi_{21} + \frac{A_{12} r_2}{r_1} \sin \psi_{12} \end{cases}$$

where $\Omega = \omega_1 - \omega_2$.

From the definition of ψ_{12} and ψ_{21} , we can see that $\dot{\theta}_{12} = \dot{\phi}_1 - \dot{\phi}_2$ and $\dot{\theta}_{21} = \dot{\phi}_2 - \dot{\phi}_1$ when the system is in a steady state (i.e. $\dot{\psi}_{12} = \dot{\psi}_{21} = 0$). In other words, the connections oscillate at the instantaneous frequency difference of the oscillators they connect. This also means that when two oscillators have different instantaneous frequencies, two connections

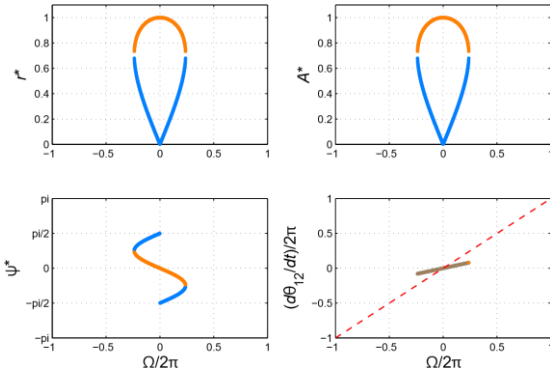


Figure 4.5. Symmetric steady-state solutions and their stability for a critical-critical coupled system ($\alpha = 0$, $\beta_1 = -1$, $\beta_2 = 0$, $\varepsilon = 0$, $\lambda = 0$, $\mu_1 = -1$, $\mu_2 = 0$, $\varepsilon_c = 0$, $\kappa = 1$).

attractors for supercritical DLC oscillators. Using the substitutions $r \equiv r_1 = r_2$, $A \equiv A_{12} = A_{21}$ and $\psi \equiv \psi_{12} = -\psi_{21}$, we get the following three-dimensional system:

$$\begin{cases} \dot{r} = \alpha r + \beta_1 r^3 + \frac{\varepsilon \beta_2 r^5}{1-\varepsilon r^2} + Ar \cos \psi \\ \dot{A} = \lambda A + \mu_1 A^3 + \frac{\varepsilon_c \mu_2 A^5}{1-\varepsilon_c A^2} + \kappa r^2 \cos \psi \\ \dot{\psi} = -\Omega - \frac{\kappa r^2 + 2A^2}{A} \sin \psi. \end{cases}$$

As we did above for oscillators with plastic coupling to external forcing, we will briefly examine different possible combinations of the regimes for oscillator and learning rule. The critical-critical system (Fig. 4.5) has stable nonzero symmetric solutions for only small values of $|\Omega|$. The symmetric steady-state behavior of a critical-supercritical system does not look much different from that of a critical-critical system. It too has nonzero stable fixed points for small $|\Omega|$ only. But note that since the learning rule is in a supercritical Hopf regime, A^* is always greater than its spontaneous amplitude. The supercritical-linear system is similar to the driven system in the same regime—a stable node for small $|\Omega|$ and a stable spiral for large $|\Omega|$. A difference between the two systems is that the coupled system shown here is unstable and blows up for small values of $|\Omega|$ when $\kappa \geq \beta_1 \lambda$. Fully expanded intrinsic damping terms with negative β_2 and μ_2 solve this problem. The supercritical-critical system shown in Fig. 4.6 has also two types of stable fixed points (nodes and spirals) but these exist for small values of $|\Omega|$. It appears, however,

that for high enough κ all unstable fixed points in the figure turn stable and become stable spirals. The supercritical-supercritical coupled system, like its driven counterpart, has stable nodes of amplitudes greater than spontaneous amplitudes for small values of $|\Omega|$ only.

Here we showed the analysis of symmetric solutions only. Numerical simulations suggest, however, that stable steady-state behaviors are always symmetric for these systems consisting of truncated canonical models of oscillators and connections. So, we did not miss any stable solutions above. Simulations also show that stable asymmetric solutions exist when supercritical

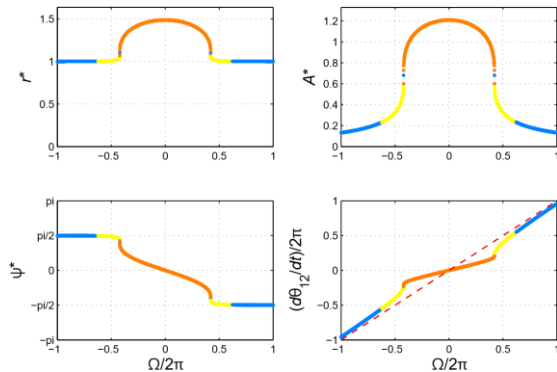


Figure 4.6. Symmetric steady-state solutions and their stability for a supercritical-critical coupled system ($\alpha = 1$, $\beta_1 = -1$, $\beta_2 = 0$, $\varepsilon = 0$, $\lambda = 0$, $\mu_1 = -1$, $\mu_2 = 0$, $\varepsilon_c = 0$, $\kappa = 0.8$).

DLC regimes are used, but analysis of the kind we did for truncated models is difficult to do for asymmetric behaviors because it requires solving the six-dimensional system with nonzero β_2 and μ_2 .

5. Computational Models of Physiological and Behavioral Data

As described in the preceding sections, we have developed a generic population-level model that is amenable to theoretical analysis. We have made significant theoretical advances in understanding signal processing, pattern formation and plasticity in networks of neural oscillators. In this section we describe how we have applied this approach to model active cochlear resonance to sound (Lerud et al., under revision), brainstem mode-locking to pitch combinations (Lerud et al., 2014), and cortical entrainment to rhythmic patterns (Large, et al., 2015).

5.1 A Canonical Nonlinear Cochlear Model

We developed and analyzed a canonical model of cochlear dynamics based on coupling between linear mechanical resonance of the basilar membrane and critical nonlinear oscillations in the organ of Corti. Through dynamical analysis, we obtain analytical forms for auditory tuning curves of both unidirectional and bidirectional systems. To validate this model we compared it with auditory nerve (AN) tuning curve data from the macaque monkey (Joris et al., 2011). We found that the model tuning curves fit the macaque data with good accuracy. A fuller description of this model is forthcoming (Lerud, Kim, Almonte, Carney & Large, under revision).

Modern models of the cochlea focus on the nonlinear oscillatory responses of outer hair cells (Julicher, 2001; Kern & Stoop, 2003). Outer hair cells poised at or near oscillatory (Hopf) instability (see Section 2) are thought to be responsible for the cochlea's extreme sensitivity, excellent frequency selectivity, and amplitude compression (Camalet, Duke, Julicher, & Prost, 1999; Eguiluz, Ospeck, Choe, Hudspeth, & Magnasco, 2000). Models of OHC nonlinearities consist of dynamical equations in the form of critical oscillators that capture generic aspects of nonlinear resonance (Fredrickson-Hemsing et al., 2012; Hoppensteadt & Izhikevich, 1997). Such models use the normal (truncated) form of the Hopf bifurcation discussed above in Section 2, (Equation 3). Equation 4 shows system behavior in terms of amplitude r and phase angle ϕ . A canonical cochlear model in which each segment of the cochlea is represented by Equation 3 (and equivalently, 4) can account for a nontrivial subset of cochlear dynamics such as sharp mechanical frequency tuning, exquisite sensitivity, and a large dynamic range (Eguiluz et al., 2000).

Starting with normal form models of outer hair cell nonlinearities as a theoretical framework, we developed an extended canonical model taking into account linear basilar membrane dynamics, critical nonlinear outer hair cell dynamics, and the coupling between the two. In the first model, linear basilar membrane oscillators drive critical nonlinear outer hair cell oscillators. In a second model, bidirectional coupling was introduced, such that the nonlinear elements reciprocally drive the linear filtering elements. Both models can be solved to determine how threshold tuning properties depend on parameters, and both models produce tuning curves that closely match responses measured in the macaque AN (Joris et al., 2011). In addition, our analysis shows that the bidirectionally coupled model produces intrinsic oscillations, such that near the empirically measured threshold there exists a bifurcation boundary between nonsynchronized and synchronized physiological responses (e.g., Johnson, 1980).

5.1.1 Unidirectional Model

We used pairs of coupled oscillators to model the dynamics of cochlear segments. In each pair, one oscillator represents BM displacement dynamics, and the other represents organ of Corti (OC) dynamics, including the outer hair cells, the tectorial membrane, and other supporting structures. Input to the complex drives the BM oscillator, which is intended to account for the dynamical effects of the cochlear fluid traveling waves that drive the BM. The OC energy source stems from critical oscillations that cause the organ of Corti to vibrate. Thus, the model exhibits both BM filtering and critical oscillations that capture the amplification, compression, and frequency selectivity of cochlear processing (Eguiluz et al., 2000).

The natural frequency of each BM-OC complex is set to correspond to the best frequency of the cochlear segment that it represents. We equate the state of the OC oscillator with the signal that is transmitted to the AN. These broad considerations lead to a coupled set of canonical oscillator equations for modeling a BM-OC complex:

$$\begin{aligned}\dot{z}_{bm} &= z_{bm} (\alpha_{bm} + i2\pi f) + F e^{i2\pi f_0 t} \\ \dot{z}_{oc} &= z_{oc} (\alpha_{oc} + i2\pi f + (\beta + i\delta)|z_{oc}|^2) + c_{21} z_{bm}\end{aligned}$$

The state variable z_{BM} represents the dynamics of the BM, while z_{OC} represents the dynamics of the OC, including the nonlinearities of the OHCs. For simplicity, we assume a linear BM. This leads to bandpass filtering behavior, making the model conceptually similar to that of (Julicher, Andor, & Duke, 2001). The linear damping parameter, $\alpha_{BM} < 0$, is determined by fitting tuning-curve data. For the OC we assume critical nonlinear oscillation, i.e., $\alpha_{OC} = 0$, resulting in optimal amplification. The nonlinear damping parameter $\beta < 0$ provides amplitude compression in the OC and is also determined by fitting tuning-curve data. Finally, the parameter c_{21} governs the relative strength of forcing of the OC by the BM and is determined by fitting the data as well.

Because the model is described in terms of the complex state variables z_{BM} and z_{OC} , it can be rewritten in polar form, giving rise to amplitude and phase equations:

$$\begin{aligned}\dot{r}_{bm} &= \alpha_{bm} r_{bm} + F \cos(2\pi f_0 t - \phi_{bm}) \\ \dot{\phi}_{bm} &= 2\pi f + \frac{F}{r_{bm}} \sin(2\pi f_0 t - \phi_{bm}) \\ \dot{r}_{oc} &= \alpha_{oc} r_{oc} + \beta r_{oc}^3 + c_{21} r_{bm} \cos(\phi_{bm} - \phi_{oc}) \\ \dot{\phi}_{oc} &= 2\pi f + \frac{c_{21} r_{bm}}{r_{oc}} \sin(\phi_{bm} - \phi_{oc}).\end{aligned}$$

Given the threshold amplitude r_{oc}^* , which is a small number that we hold constant across tuning curves, the formula for F only in terms of model parameters is

$$F = \frac{r_{oc}^*}{c_{21}} \left(\alpha_{bm}^2 + \Omega^2 \right)^{\frac{1}{2}} \left(\alpha_{oc}^2 + 2r_{oc}^{*2} \alpha_{oc} \beta + r_{oc}^{*4} \beta^2 + \Omega^2 + 2\Omega \delta r_{oc}^{*2} + \delta^2 r_{oc}^{*4} \right)^{\frac{1}{2}}$$

F is normally in pascals which can then be converted to the stimulus level L in dB SPL by $L = 20 \log(F/p_0) - G$, where $p_0 = 20 \mu\text{Pa}$ represents the reference pressure, and G the gain of the middle ear filter in dB.

To determine tuning curves that can be compared with auditory-nerve data, we first pass the acoustic stimulus through a linear filter to approximate the amplitude and phase response of the middle ear (Bruce, Sachs, & Young, 2003; Zilany & Bruce, 2006). The middle-ear filter is a simplified form of that of Bruce (2003). Zilany and Bruce developed a fifth-order continuous-time transfer function and represented it as a fifth-order digital filter using a bilinear transformation for a sampling frequency of 500 kHz, with the frequency axis pre-warped to give a matching frequency response at 1 kHz. To ensure stability of the digital filter, it was implemented in a second-order system form by cascading digital filters. Once the MEF and cochlear BM-OC oscillatory complexes are defined, the resulting waveform is provided as input.

The three parameters, $\alpha_{BM} < 0$, $\beta < 0$, and $c_{21} > 0$, are determined using a search procedure that adjusts model parameters to obtain a sufficiently close match to the data. We held the threshold $r^*_{OC} = 0.1$ constant and fit each curve individually. The results of the parameter searches are shown in green in Figure 5.1 A, B, and C, for low, mid, and high frequency tuning curves from the Joris et al. data set, respectively. The average root-mean-square error for the fits in was 6.9219 dB. It was noted that both α_{BM} and β varied within a single order of magnitude over all tuning curves, and c_{21} was a reliable linear function of CF.

5.1.2 Bidirectional Model

A more realistic configuration of the BM-OC oscillatory complexes is to use bidirectional coupling between the two oscillators rather than unidirectional coupling used in the previous model. Thus, our second model considers the effect of OC dynamics on the BM. With bidirectional coupling, the dynamics of an oscillatory complex are governed by

$$\begin{aligned}\dot{z}_{bm} &= z_{bm} (\alpha_{bm} + i2\pi f) + Fe^{i2\pi f_0 t} + c_{12}z_{oc} \\ \dot{z}_{oc} &= z_{oc} (\alpha_{oc} + i2\pi f + (\beta + i\delta)|z_{oc}|^2) + c_{21}z_{bm},\end{aligned}$$

with c_{12} being the coupling coefficient of the OC oscillator feeding back to the BM oscillator. Similarly to the unidirectional model, we can get a closed-form formula for forcing amplitude F expressed as a function of threshold amplitude r^*_{OC} , frequency difference Ω , and model parameters:

$$F = \sqrt{(\alpha_{bm}r^*_{bm} + c_{12}r^*_{oc} \cos \psi^*_{oc})^2 + (\Omega r^*_{bm} + c_{12}r^*_{oc} \sin \psi^*_{oc})^2}$$

where

$$\begin{aligned}r^*_{bm} &= \frac{r^*_{oc}}{c_{21}} \sqrt{(\alpha_{oc} + \beta r^*_{oc})^2 + (\Omega + \delta r^*_{oc})^2}, \\ \sin \psi^*_{oc} &= \frac{r^*_{oc} (\Omega + \delta r^*_{oc})}{c_{21}r^*_{bm}}, \quad \text{and} \\ \cos \psi^*_{oc} &= \sqrt{1 - \sin^2 \psi^*_{oc}}\end{aligned}$$

Stability analysis of this system reveals that bidirectional coupling introduces an important change in the dynamics of BM-OC complexes. With unidirectional coupling and with α_{BM} set to zero or below, both the BM and OC oscillators decay to zero when not driven by external forcing. With bidirectional coupling, however, the two oscillators provide input to each other and as a

result they have nonzero steady-state amplitudes even in the absence of external forcing. A consequence of having nonzero spontaneous amplitude is that a BM-OC complex with bidirectional coupling may not phase-lock to external forcing if its natural frequency is too different from forcing frequency or if forcing is not strong enough. Figures 5.1D,E&F show resonance regions or “Arnold tongues” for a bidirectional model within which the model phase-locks to external forcing. Steady-state solutions (or fixed points) may exist outside the resonance region, but they are not stable (i.e., the model is not attracted to them). Typically, steady-state amplitudes r^*_{OC} and r^*_{BM} are unstable when they are smaller than the spontaneous amplitudes. In comparison, a BM-OC complex with unidirectional coupling and $\alpha_{OC} \leq 0$ phase-locks to external forcing of any frequency and amplitude.

Due to the possibility of unstable solutions for bidirectional models, the forcing amplitude F should be examined for its stability when the threshold amplitude r^*_{OC} set below the spontaneous amplitude of z_{OC} . To compare tuning in this model to the tuning in the unidirectional model, we choose the coupling, C_{12} , such that spontaneous amplitude is just below threshold amplitude, $r^*_{OC} = 0.1$. Figure 5.1 D,E&F show the

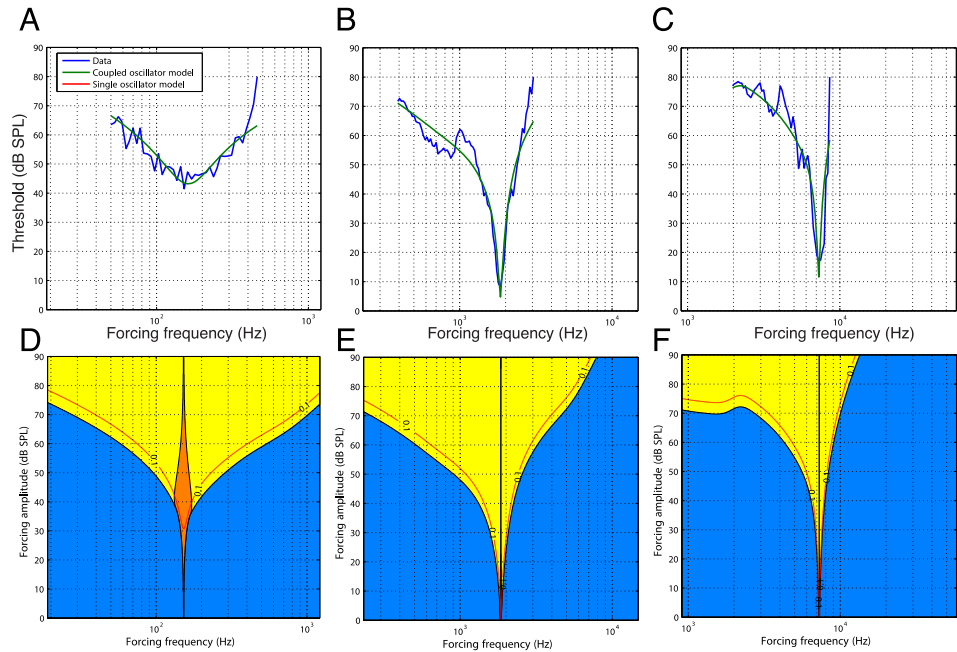


Figure 5.1. Top: Fits of the unidirectional model to low (A), mid (B), and high (C) frequency AN fibers from the Joris (2001) data set. Data is in blue, model fits are in green. Bottom: Resonance regions of the bidirectional model for low (D), mid (E), and high (F) frequency AN fibers, using the same parameters. Coupling from OC to BM, was chosen so that spontaneous amplitude was slightly below threshold amplitude, $r^*_{OC} = 0.1$. The red contours show threshold amplitude. The BM-OC model phase-locks to external forcing in the parameter regions where the fixed point is either a stable node (red) or a stable spiral (yellow). Non-phase locked regions (saddle points) are shown in blue.

tuning curves (red) lie just above the phase-locking boundary, and are similar to the tuning curves for the unidirectional model. The bidirectional model did not provide significantly better fits to the tuning-curve data. However, the bidirectional model makes the important prediction that cochlear and AN phase-locking will be observed before amplitude of firing frequency increases significantly. This prediction matches empirical observations (e.g., Johnson, 1980). Another important feature of this bidirectional model is spontaneous oscillation. It is well known that many mammalian cochleae exhibit spontaneous otoacoustic emissions, and this aspect of auditory nonlinearity cannot be predicted with a unidirectionally coupled model.

Summary: Nonlinear responses to acoustic signals arise through active processes in the cochlea, whose exquisite sensitivity and wide dynamic range can be explained by critical nonlinear oscillations of hair cells. We studied how the interaction of critical nonlinearities with

the basilar membrane and other organ of Corti components could determine tuning properties of the mammalian cochlea. We developed a canonical model in which the dynamics of the basilar membrane–organ of Corti interaction is captured using pairs of coupled oscillators tuned to a gradient of natural frequencies. We first developed a minimal model in which a linear oscillator, representing basilar membrane dynamics, is coupled to a nonlinear oscillator poised at a Hopf instability, which captures the nonlinear responses of outer hair cells and related organ of Corti components. Parameters were determined by fitting the auditory-nerve tuning curves of macaque monkeys. We then developed a more sophisticated model, taking into account bidirectional coupling. We found that the unidirectionally and bidirectionally coupled models account equally well for threshold tuning, but the bidirectionally coupled model also exhibited low amplitude, spontaneous oscillation, providing a model that phase-locks to sound.

5.2 Brainstem Processing of Pitch Combinations

While some nonlinear responses arise through active processes in the cochlea, others arise in neural populations of the cochlear nucleus, inferior colliculus and higher auditory areas. Recently mode-locking, a generalization of phase locking that implies an intrinsically nonlinear processing of sound, has been observed in mammalian auditory brainstem nuclei. We developed a canonical model of mode-locked neural oscillation in brainstem that predicts the complex nonlinear population responses to musical intervals that have been observed in the human brainstem (for complete details, see Lerud et al., 2014).

In central auditory circuits, action potentials phase-lock to both the fine time structure and the temporal envelope modulations of auditory stimuli at many different levels, including cochlear nucleus, superior olive, inferior colliculus, thalamus, and A1 (Langner, 1992). Traditionally, phase-locked spiking in the central auditory system is thought to represent an essentially passive transmission of synchronized basilar membrane motion. An alternative possibility is that active circuits in the central auditory system carry synchronized neural activity forward. If this is the case, nonlinearities observed at the level of the brainstem might also arise due to mode-locking (see Section 3), a phenomenon that has been observed in the auditory brainstem (Langner, 1992), and is physiologically distinct from the mechanical compression and half-wave rectification that occurs in the organ of Corti.

Mode-locking to acoustic signals has been observed in guinea pig cochlear nucleus chopper and onset neurons (Laudanski et al., 2010), and mode-locking to the difference tone of two dichotically presented stimulus frequencies has been observed *in vivo* and isolated to the inferior colliculus of the chinchilla (Arnold and Burkard, 1998, 2000). Mode-locked spiking patterns are often observed *in vitro* under DC injection (Brumberg and Gutkin, 2007), and active oscillations have been observed *in vivo* in the inferior colliculus of the chicken (Schwarz et al., 1993). Such observations lead to the possibility that the nonlinear responses observed in the human auditory brainstem might arise, in part, due to mode-locking neurodynamics.

We modeled nonlinear responses to musical intervals that have been measured in the human auditory brainstem response (Lee et al., 2009, see Fig. 2). In that study, the brainstem representation of the musical intervals comprised not only stimulus frequencies, but also numerous resonances at frequencies that were not physically present in the stimulus. How did these frequencies arise? The stimuli were the intervals major sixth (G and E, “consonant”) and minor seventh (F# and E, “dissonant”) which have fundamental frequency ratios of 1.6 (166 Hz/99 Hz) and 1.7 (166 Hz/93 Hz), making it unlikely that interaction of the fundamental frequencies created strong distortion products in the cochlea (Dhar et al., 2009, 2005; Knight and Kemp, 2001). Moreover, the responses of trained musicians were significantly enhanced

compared with those of novice listeners, implying experience- based differences that would not have arisen at the level of the cochlea or auditory nerve (e.g., Large, Kozloski, & Crawford, 1998; Laudanski et al., 2010).

The stimuli from the Lee et al. (2009) study were used as input to a cochlear model (see Section 5.1), which in turn provided input to two brainstem network layers. The characteristic frequencies of the cochlear layer and both brainstem layers spanned four octaves with 99 oscillators per octave. Thus, each layer included 397 oscillators, with characteristic frequencies ranging from 64 Hz to 1024 Hz, encompassing the range of frequencies for which time-locked responses have been observed in midbrain physiology (Langner, 1992). The cochlear model includes a middle ear filter and simulates the basilar membrane and the organ of Corti (cf. Jülicher et al., 2001 B). The cochlea is connected to the first brainstem layer, representing the cochlear nucleus (CN), and the CN is connected to the second brainstem layer, representing the inferior colliculus/ lateral lemniscus (IC/LL).

We modeled FFRs from Lee et al., responses to both the consonant and dissonant intervals. The stimulus was input to the cochlea, all oscillator equations were numerically integrated for the length of the stimulus, and the responses in all layers were stored. To compute the model brainstem FFR, the responses of all oscillators in each layer were averaged, leaving a single time series for each layer. The model FFR was a weighted average of the cochlea, CN, and IC/LL

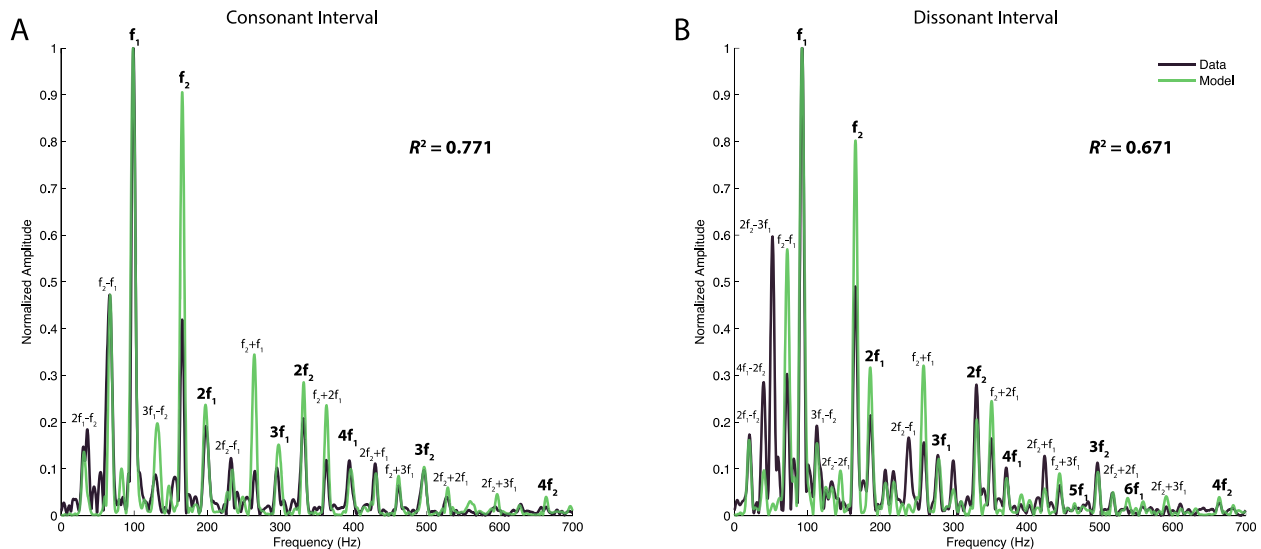


Figure 5.2. Comparisons of model predictions and auditory brainstem responses of nonmusicians to (A) the consonant interval (99 Hz, 166 Hz) and (B) the dissonant interval (93 Hz, 166 Hz). The labels above each spectral component refer only to their specific frequencies as functions of the primaries, and do not necessarily reflect the generating processes of those components.

layers. This weighted average was filtered (3rd-order digital Butterworth low-pass, 450 Hz cutoff) to account for the lowpass effect of the skull, meninges, and scalp on the FFR. Finally, the resultant model time series were averaged and fast Fourier transformed to produce a model fit. The model fits, for the consonant and dissonant intervals were optimized with a single degree of freedom through a series of simulations. In the simulations, the parameter ϵ (Equation 1) was systematically varied between zero and one to yield the highest correlation for each fit.

Fig. 5.2 shows the predicted brainstem responses. The canonical population response predicts each peak in the brainstem response with remarkable accuracy for both intervals (consonant: $R^2=0.77$, $p<0.0001$; dissonant: $R^2=0.67$, $p<0.0001$). The more subtle differences could not be accounted for by manipulation of ϵ alone, implying that incorporation of other

network properties into the model, i.e., synaptic coupling, will be necessary to explain the responses of listeners. This is consistent with the interpretation that the refinement of auditory sensory encoding is driven by synaptic plasticity that links learned representations to the neural encoding of acoustic features (Lee et al., 2009).

Summary: A single parameter of a model brainstem network was manipulated to fit Lee et al.'s (2009) brainstem FFR data. The parsimony of the model, its basis in neurophysiological observations of mode-locking, and the quality of the fits all speak to the potential of this theoretical approach. We are currently developing improvements to enable more comprehensive simulations of the early auditory system that include all relevant aspects of cochlear dynamics, as well as parameterization of CN and IC/LL dynamics. In comprehensive models, parameter fitting is a significant issue. We are also exploring models of synaptic plasticity for neural oscillator networks (see Equation 2 and Section 4) in order to better explain the responses of trained listeners. This approach may lead to an understanding of general neural signal processing principles underlying music and pitch perception. Moreover, canonical analysis of plasticity in neural oscillator networks may help us to understand the role of learning in modulating these responses.

5.3 Cortical Synchronization to Complex Rhythms

We have developed a model that makes detailed, quantitative predictions about cortical population rhythms hypothesized to underlie human rhythm perception. We directly tested the predictions in behavioral and neurophysiological experiments. In particular, our model makes predictions about the perception of pulse and meter in complex rhythms as well as activity within auditory and motor systems.

Pulse and meter perception arise from complex interactions within a widespread auditory-motor network (Lee, Skoe, Kraus, & Ashley, 2009). EEG and MEG studies have directly tested the neural dynamics that emerge during rhythm perception. One group of studies has looked at how steady state evoked potentials (SS-EP) are affected by pulse perceptions and by different tempi. Will and Berg (e.g., Chen, Penhune, & Zatorre, 2008; Grahn & Rowe, 2009) reported substantial SS-EP responses to isochronous stimuli, but only in the delta/theta range, with the strongest SS-EP response for 2Hz stimuli, a rate which corresponds to the optimal pulse-tempo identified in numerous listening, tapping synchronization, and event-interval discrimination experiments (2007). Another study found that while periodic rhythm elicited a sustained response at the rate of the stimulus, meter imagery elicited an additional subharmonic resonance corresponding to the metric structural interpretation (McAuley & Jones, 2003). Similarly, the amplitude of the SS-EPs at pulse and meter frequencies of complex rhythms is selectively enhanced (S. Nozaradan et al., 2011). While these studies support the notion that neural activity synchronizes to rhythms, synchronization cannot be unambiguously attributed to oscillatory entrainment because they do not rule out the possibility that SS-EPs may be driven bottom-up by the stimulus itself.

Other EEG/MEG studies have demonstrated synchronization of high-frequency power modulations (in the beta/gamma-band range 15-50Hz) to the temporal structure of sounds. One EEG study found that fluctuations in induced beta- and gamma-band power synchronized with periodic and metrical rhythms, and was unaltered even when sounds were omitted, emphasizing its top-down anticipatory (rather than bottom-up reflexive) nature (Sylvie Nozaradan, 2012). Similarly, MEG studies found anticipatory induced beta-band responses for periodic and metrical sequences, but not for randomly timed sequences (Snyder & Large, 2005), and subharmonic responses were observed in induced beta band activity when subjects were instructed to impose a

subjective meter on a periodic stimulus, closely resembling those produced by physical accents (Fujioka, Large, Trainor, & Ross, 2009). MEG source analysis has revealed beta-band interactions in auditory and motor networks during musical rhythm processing (Iversen, Repp, & Patel, 2009). Given the role of beta in motor processing and long-range intra-cortical interaction, these findings are consistent with the idea that the motor system influences the perception of sound, even in the absence of overt movement. Thus, beta and gamma band responses to auditory rhythms as well as SS-EPs are in line with the basic prediction that neural rhythms synchronize to the pulse.

While empirical observations demonstrate neural synchrony, the hypothesis of entrained neuronal oscillation remains controversial. The most straightforward objection is that 1) apparent entrainment of SS-EPs reflects overlapping of transient responses such as the N1-P2 complex (Sussman, Steinschneider, Gumenyuk, Grushko, & Lawson, 2008; Tremblay, Billings, & Rohila, 2004). A related possibility is that 2) observed synchrony may be a passive response, like that of a linear band-pass filter. If synchrony is passive then 3) observed neural processes would not be capable of the cognitive computations necessary for structure perception (Patel & Iversen, 2014). Fortunately, it is possible to identify active responses because entrainment reflects interaction of the stimulus with intrinsic neural dynamics.

5.3.1 The Auditory-Motor Resonance Model

We used two gradient frequency networks (see Equation 1) to model the functional coupling of auditory-motor networks observed in rhythm perception tasks without a motor component. The sensory network is intended to capture auditory cortical entrainment, while the motor network is intended to capture the dynamics of a broadly distributed network including basal ganglia and cortical areas. The sensory network takes a rhythmic input, sends output to a motor network, and the motor network send input back to the sensory network (Large et al., 2015). Connections within and between networks are assumed to be plastic and tuned by musical enculturation (cf., Hannon and Trehub, 2005; see also Section 4).

Although the model makes only general assumptions regarding underlying neural structures (e.g., Chen et al., 2008), it makes strong commitments about the oscillatory dynamics of auditory-motor interactions (Will and Berg, 2007; Fujioka et al., 2012; Nozaradan et al., 2013). The sensory oscillators are tuned to operate near a Hopf bifurcation; the motor oscillators are tuned to operate near a double limit cycle bifurcation (see Section 2). The double limit cycle

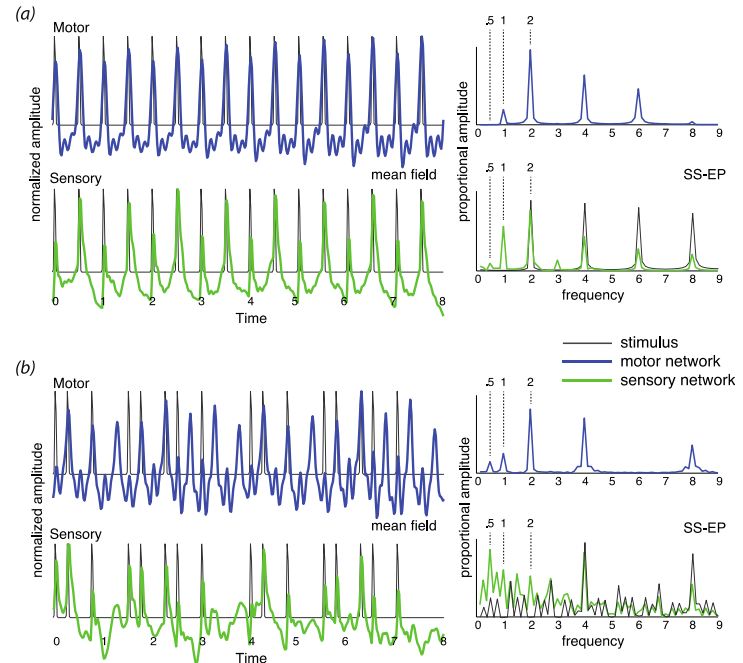


Figure 5.3. The network was stimulated with (a) an isochronous rhythm and (b) a “missing pulse” rhythm. Output of the sensory network is in green and output of the motor network is in blue. The mean field time series (left) was obtained by summing the output of all the oscillators in the network over time. The SS-EP was obtained by Fourier analysis (FFT) of the mean field time series. The Fourier analysis (FFT) of the stimulus envelope is shown in black on the sensory SS-EP axis.

regime of the motor network means that the model can capture synchronization-continuation behavior, continuing to produce rhythmic behavior after the stimulus. To predict mean field time series as observed in EEG recordings (e.g., Will and Berg, 2007; Stefanics et al., 2010), we sum the output of all oscillators in each network (Figure 5.3, left). To predict steady state evoked potentials (SS-EPs) we take a frequency analysis (DFT) of the mean field (Figure 5.3, right).

As shown in Figure 5.3A, for a periodic stimulus, both sensory and motor networks produce synchronized oscillations at the pulse frequency, and generate harmonics (Repp, 2008) and subharmonics (Vos, 1973; Bolton, 1894; Nozaradan et al., 2011). In the case of a complex rhythm, however, it becomes clear that the two networks are doing something quite different from one another. The mean field time trace for the sensory network represents the input rhythm rather faithfully, producing well-defined pulses at input event times. By contrast, the motor network entrains at the pulse frequency. The rhythm itself contains no energy at the pulse frequency (or its second subharmonic; DFT in Figure 5.3B, SS-EP, solid black), however, in the motor network the strongest response is found at the pulse frequency. In other words, the development of the pulse percept depends on the interaction of these two oscillatory systems.

This predicts that an oscillatory network interaction can lead to spontaneous pulse induction in complex rhythms—even in the most extreme case of a rhythm for which there is no energy at the pulse frequency. Thus, the theoretical prediction is that pulse may be perceived at a frequency that is not physically present in the rhythmic stimulus (Large, 2010; Velasco and Large, 2011).

5.3.2 Behavioral Data

To test behavioral predictions, we asked participants to listen to eleven rhythms ranging from isochronous to highly complex. Participants were instructed to listen to each rhythm until they heard a steady pulse, and then tap along with the rhythm at that rate. Rhythms were presented at five levels of complexity (0–4) and at five different tempi (i.e., pulse frequencies): 2.28 Hz (420 ms), 2.17 Hz (460 ms), 2 Hz (500 ms), 1.85 Hz (540 ms), and 1.72 Hz (580 ms). The simplest rhythms (complexity 0) were isochronous, the most complex rhythms contained no

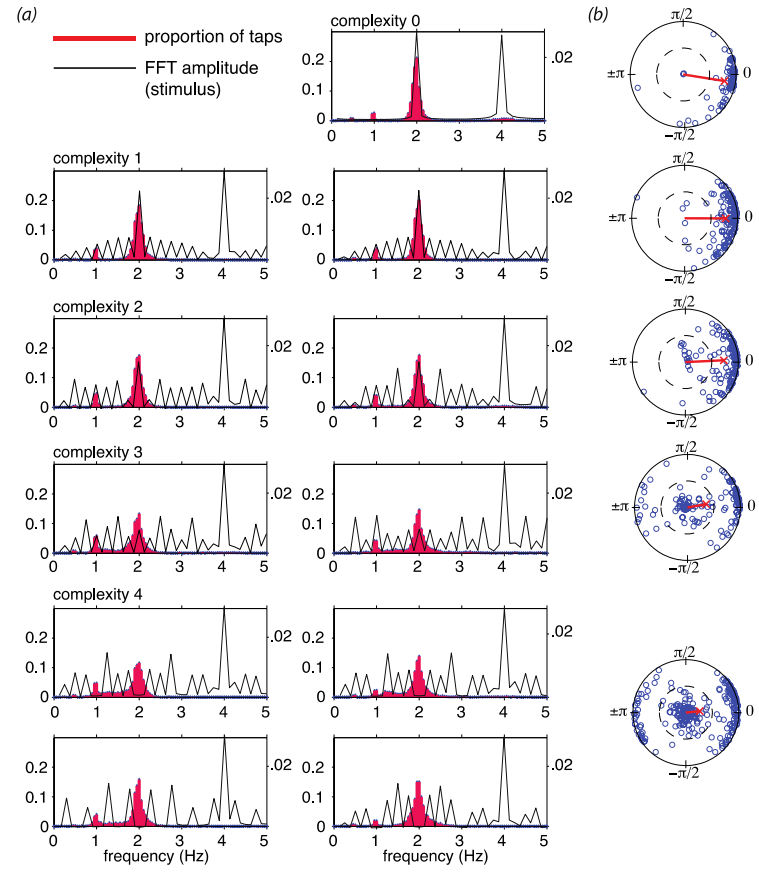


Figure 5.4. (a) Tapping frequencies were normalized to 2 Hz to allow comparison between trials at different tempos. Tapping frequency distributions (red histograms) were computed by binning normalized instantaneous tapping frequencies from 0 Hz to 5.00 Hz in bins widths of 0.05 Hz. Distributions were computed for each rhythm separately, including every tap interval across trials. Black lines show amplitude spectrum of the stimulus envelope for comparison. (b) Circular means of tap phases for each trial (blue circles) and grand mean for each complexity level (red line).

spectral energy at the pulse frequency (complexity 4). Different combinations of tempo and rhythm were presented in a pseudorandom order such that consecutive trials always had different rhythms, and different tempos. Thus, participants were forced to find both the frequency and the phase of the pulse anew for each rhythm; they could not simply tap at the same tempo throughout the experiment.

We measured instantaneous tapping frequency distributions to determine whether subjects induced a pulse at the intended frequency. Instantaneous tapping frequency was computed as $1/ITI$ (ITI = inter-tap interval in seconds) and tapping frequencies were normalized to a frequency of 2 Hz so they could be combined into a single distribution at each level of complexity. Spectral analysis (DFT) of the stimulus rhythms (Figure 5.4A, black) shows that at the hypothetical pulse frequency amplitude decreases with increasing complexity. At complexity level 4, the amplitude is precisely zero at 2 and 1 Hz for each rhythm. Normalized instantaneous tapping frequency (Figure 5.4A, red histogram) displays a main peak at the normalized pulse frequency of 2Hz for all rhythms at all levels of complexity, with lesser peaks at 1 and 0.5Hz, and for some rhythms, a diffuse peak around 4Hz. Thus, the participants most often tapped the predicted pulse frequency even for the most complex rhythms, which had no spectral amplitude at that frequency.

Next, we examined synchronization for each trial. The sequence of tap times was converted into a sequence of phases relative to the predicted pulse frequency, and the circular mean was computed for each trial (Batschelet, 1981; Figure 5.4B; blue circles). The grand mean was then computed for each complexity level (Figure 5.4B, red line). As predicted by the model, participants synchronized—either in-phase or anti-phase—predominantly at the missing pulse frequency. This behavior is consistent with the prediction that formation of the pulse percept arises due to entrainment of emergent neuronal oscillations. It also rules out the potential alternatives that synchronization is merely a consequence of a common rhythmic input, or that the pulse percept may arise due to linear resonance. Theoretically speaking, it is critical to distinguish the role of a common stimulus frequency from the intrinsic dynamics of an emergent oscillation (Whittington et al., 2000), and the missing pulse rhythms used here enabled us to dissociate the two.

5.3.3 Neural Data

The theoretical model also makes strong physiological predictions that must also be put to empirical test. The prediction is that in listening to these ‘missing pulse’ rhythms, the pulse frequency will be observed in auditory and motor activity despite its absence from the stimulus acoustics. Fig 5.5 shows MEG data from $n=8$ participants, listening passively to two of the complex ‘missing pulse’ stimuli (MP1 and MP2) used in the model simulations (Tal et al, submitted). The spectra of responses from right and left auditory cortices show the emergence of peaks at the 2Hz ‘missing pulse’ (and in one case its 1Hz subharmonic; $p<0.05$ for all relative to adjacent frequencies; regions of interest selected based on an independent auditory

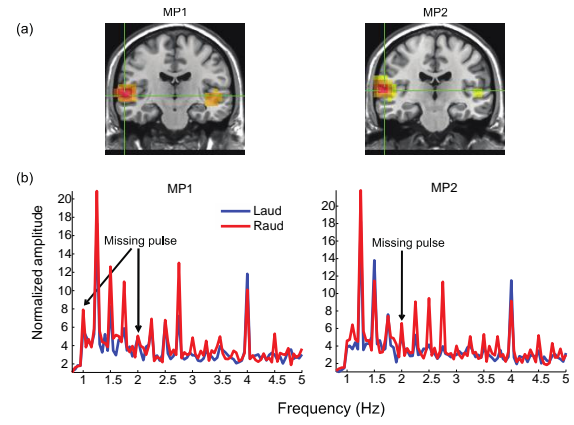


Figure 5.5. (a) Synchronized neural activity was found in left and right auditory cortices in response to both complex rhythms. (b) Energy was found at the missing pulse (here, 2 Hz) and its second subharmonic (1 Hz) consistent neither of which were present in the stimuli.

localizer task; Source localization performed using SAM beamforming). Moreover, we found that the magnitude of the ‘missing pulse’ response is correlated with pulse perception across individuals, such that participants who perceived the pulse quickly had stronger responses than participants who took longer to perceive a pulse (MP1: $r=-0.81$, $p<0.005$; MP2: $r=-0.6$, $p<0.05$; data not shown). These findings confirm the falsifiable physiological predictions of the model, they show that neural frequencies correspond to listener’s perceptions, and they conclusively rule out transient or passive explanations of neural synchrony. Thus, this experiment provided strong evidence for the viability of the model as a theoretical framework for explaining rhythm perception.

Summary: We have made significant progress in understanding the role of neural oscillations and the neural structures that support synchronized responses to musical rhythm. Our neurodynamic model that shows how self-organization of oscillations in interacting sensory and motor networks could be responsible for the formation of the pulse percept in complex rhythms. In a pulse synchronization study, we tested the model’s key prediction that pulse can be perceived at a frequency for which no spectral energy is present in the amplitude envelope of the acoustic rhythm. The result shows that participants perceive the pulse at the theoretically predicted frequency. Synchronized neural activity consistent with model predictions has also been observed in auditory cortex, providing strong evidence for the viability of this theoretical framework for explaining rhythm perception. Our model is one of the few consistent with neurophysiological evidence on the role of neural oscillation, and it explains a phenomenon that other computational models fail to explain. Because it is based on a canonical model, the predictions hold for an entire family of dynamical systems, not only a specific one. Thus, this model provides a theoretical link between oscillatory neurodynamics and the induction of pulse and meter in musical rhythm.

6. Concluding Remarks

In this project, we developed a theoretical framework for auditory neural processing and auditory perception. We modeled the auditory system as a dynamical system consisting of oscillatory networks, and auditory perception as stable dynamic patterns formed in the networks in response to acoustic signals. We developed GrFNNs, generic models that capture the neurocomputational properties of a family of neurophysiological models using bifurcation theory. We made significant progress in understanding the signal processing, pattern formation and plasticity in GrFNNs. We developed three models that exploit these properties to model important aspects of auditory neurophysiology and auditory perception. Future modeling efforts based on canonical dynamical systems could bring us closer to understanding fundamental mechanisms of hearing, communication, and auditory system development.

In addition to these accomplishments, we produced a computational framework for GrFNNs in Matlab, sped up our computational simulations using GPU acceleration, and created a C++ version of the GrFNN code to develop end-user applications that run on CPUs, GPU, mobile platforms and embedded devices. We anticipate that this computational framework will power the next generation of auditory processing hardware and software. In ongoing work, we are exploring the abilities of such networks to address the auditory scene analysis problem.

Bibliography

Aronson, D. G., Ermentrout, G. B., & Kopell, N. (1990). Amplitude response of coupled oscillators. *Physica D: Nonlinear Phenomena*, 41(3), 403-449.

Bruce, I. C., Sachs, M. B., & Young, E. D. (2003). An auditory-periphery model of the effects of acoustic trauma on auditory nerve responses. *The Journal of the Acoustical Society of America*, 113(1), 369-388.

Brunel, N. (2000). Dynamics of sparsely connected networks of excitatory and inhibitory spiking neurons. *Journal of Computational Neuroscience*, 8(3), 183-208.
doi:papers2://publication/uuid/A7D84CF5-49C7-41FF-BCDB-B552A936F0F5

Camalet, S., Duke, T., Julicher, F., & Prost, J. (1999). Auditory sensitivity provided by self tuned critical oscillations of hair cells. *Proceedings of the National Academy of Sciences USA*, 97, 3183-3188.

Chen, J. L., Penhune, V. B., & Zatorre, R. J. (2008). Listening to Musical Rhythms Recruits Motor Regions of the Brain. *Cerebral Cortex*, 18(12), 2844-2854.
doi:10.1093/cercor/bhn042

Childs, L. M., & Strogatz, S. H. (2008). Stability diagram for the forced Kuramoto model. *Chaos*, 18(4), 043128. doi:papers2://publication/doi/10.1063/1.3049136

Eguíluz, V. M., Ospeck, M., Choe, Y., Hudspeth, A. J., & Magnasco, M. O. (2000). Essential nonlinearities in hearing. *Physical Review Letters*, 84(22), 5232.

Fredrickson-Hemsing, L., Ji, S., Bruinsma, R., & Bozovic, D. (2012). Mode-locking dynamics of hair cells of the inner ear. *Physical Review E*, 86(2), 021915.
doi:papers2://publication/doi/10.1103/PhysRevE.86.021915

Fujioka, T., Large, E. W., Trainor, L. J., & Ross, B. (2009). Beta and gamma rhythms in human auditory cortex during musical beat processing. The Neurosciences and Music III: Disorders and Plasticity. *Annals of the New York Academy of Sciences*, 1169, 89-92.

Grahn, J. A., & Rowe, J. B. (2009). Feeling the beat: premotor and striatal interactions in musicians and non-musicians during beat processing. *Journal of Neuroscience*.

Holmes, P. J., & Rand, D. A. (1978). Bifurcations of the forced van der Pol oscillator. *Quarterly of Applied Mathematics*, 35, 495-509.

Hoppensteadt, F. C., & Izhikevich, E. M. (1996). Synaptic organizations and dynamical properties of weakly connected neural oscillators II: Learning phase information. *Biological Cybernetics*, 75, 126-135.

Hoppensteadt, F. C., & Izhikevich, E. M. (1997). *Weakly Connected Neural Networks*. New York: Springer.

Iversen, J. R., Repp, B., & Patel, A. D. (2009). Top-down control of rhythm perception modulates early auditory responses The Neurosciences and Music III: Disorders and Plasticity. *Annals of the New York Academy of Sciences*, 1169, 58-73.

Johnson, D. H. (1980). The relationship between spike rate and synchrony in responses of auditory-nerve fibers to single tones. *The Journal of the Acoustical Society of America*, 68(4), 1115-1122. doi:papers2://publication/uuid/CC732D14-61C3-4F7C-91FE-FDF0B533669C

Joris, P. X., Bergevin, C., Kalluri, R., Mc Laughlin, M., Michelet, P., van der Heijden, M., & Shera, C. A. (2011). Frequency selectivity in Old-World monkeys corroborates sharp cochlear tuning in humans. *Proceedings of the National Academy of Sciences*.

Julicher, F. (2001). Mechanical oscillations at the cellular scale. *Comptes Rendus De L Academie Des Sciences Serie Iv Physique Astrophysique*, 2(6), 849-860.

Julicher, F., Andor, D., & Duke, T. (2001). Physical basis of two-tone interference in hearing. *Proceedings of the National Academy of Sciences of the United States of America*, 98(16), 9080-9085.

Kern, A., & Stoop, R. (2003). Essential role of couplings between hearing nonlinearities. *Physical Review Letters*, 91(12), 128101(128104).

Kim, J. C., & Large, E. W. (2015). Signal Processing in Periodically Forced Gradient Frequency Neural Networks. *Frontiers in Computational Neuroscience*, 9, 152. doi:papers2://publication/doi/10.3389/fncom.2015.00152

Langner, G. (1992). Periodicity coding in the auditory system. *Hearing Research*, 60, 115-142.

Large, E. W., Almonte, F., & Velasco, M. (2010). A canonical model for gradient frequency neural networks. *Physica D: Nonlinear Phenomena*, 239(12), 905-911. doi:10.1016/j.physd.2009.11.015

Large, E. W., Herrera, J. A., & Velasco, M. J. (2015). Neural Networks for Beat Perception in Musical Rhythm. *Frontiers in Systems Neuroscience*, 9(224), 583. doi:papers2://publication/doi/10.1152/jn.00066.2009

Large, E. W., Kozloski, J., & Crawford, J. D. (1998). A dynamical model of temporal processing in the fish auditory system. *Association for Research in Otolaryngology Abstracts*, 21(236), 717.

Laudanski, J., Coombes, S., Palmer, A. R., & Sumner, C. J. (2010). Mode-locked spike trains in responses of ventral cochlear nucleus chopper and onset neurons to periodic stimuli. *Journal of Neurophysiology*, 103(3), 1226-1237. doi:Doi 10.1152/jn.00070.2009

Lee, K. M., Skoe, E., Kraus, N., & Ashley, R. (2009). Selective subcortical enhancement of musical intervals in musicians. *Journal of Neuroscience*, 29(18), 5832-5840.

Lerud, K. D., Almonte, F. V., Kim, J. C., & Large, E. W. (2014). Mode-locking neurodynamics predict human auditory brainstem responses to musical intervals. *Hearing Research*. doi:papers2://publication/doi/10.1016/j.heares.2013.09.010

Lerud, K. D., Kim, J. C., Almonte, F. V., Carney, L. H., & Large, E. W. (under revision). A canonical nonlinear cochlear model. doi:papers2://publication/uuid/E91A62EA-9977-4D01-9F5E-2267A8277915

McAuley, J., & Jones, M. R. (2003). Modeling effects of rhythmic context on perceived duration: a comparison of interval and entrainment approaches to short-interval timing. *J Exp Psychol Hum Percept Perform.*, 29(6), 1102-1125.

Meddis, R., & O'Mard, L. P. (2006). Virtual pitch in a computational physiological model. *The Journal of the Acoustical Society of America*, 120(6), 3861-3869. doi:papers2://publication/uuid/C44D129E-23E4-40ED-86F1-DC65B9494343

Nozaradan, S. (2012). Selective neuronal synchronization to the beat and meter embedded in a musical rhythm. doi:papers2://publication/uuid/067E72DD-9FD6-466E-B059-7060BEFA5402

Nozaradan, S., Peretz, I., Missal, M., & Mouraux, A. (2011). Tagging the neuronal entrainment to beat and meter. *Journal of Neuroscience*, 31(28), 10234-10240.

Patterson, R. D., Robinson, K., Holdsworth, J., McKeown, D., Zhang, C., Allerhand, M., . . . Langner, G. (1992). Complex Sounds and Auditory Images. *Auditory Physiology and Perception*, 83, 429-446.

Snyder, J. S., & Large, E. W. (2005). Gamma-band activity reflects the metric structure of rhythmic tone sequences. *Cognitive Brain Research*, 24(1), 117-126.

Stefanescu, R., & Jirsa, V. (2008). A Low Dimensional Description of Globally Coupled Heterogeneous Neural Networks of Excitatory and Inhibitory Neurons. *PLoS Computational Biology*, 4(11), e1000219.

Sussman, E., Steinschneider, M., Gumenyuk, V., Grushko, J., & Lawson, K. (2008). The maturation of human evoked brain potentials to sounds presented at different stimulus rates. *Hearing Research*, 236(1–2), 61-79.
doi:<http://dx.doi.org/10.1016/j.heares.2007.12.001>

Tremblay, K., Billings, C., & Rohila, N. (2004). Speech evoked cortical potentials: effects of age and stimulus presentation rate. *J Am Acad Audiology*, 15(3), 226-237.

Will, U., & Berg, E. (2007). Brain wave synchronization and entrainment to periodic acoustic stimuli. *Neuroscience Letters*, 424(1), 55-60.
doi:<http://dx.doi.org/10.1016/j.neulet.2007.07.036>

Zilany, M. S., & Bruce, I. C. (2006). Modeling auditory-nerve responses for high sound pressure levels in the normal and impaired auditory periphery. *Journal of the Acoustical Society of America*, 120(3), 1446.

AFOSR Deliverables Submission Survey

Response ID:7198 Data

1.

Report Type

Final Report

Primary Contact Email

Contact email if there is a problem with the report.

ed@circular-logic.com

Primary Contact Phone Number

Contact phone number if there is a problem with the report

860-282-4215

Organization / Institution name

Circular Logic LLC

Grant/Contract Title

The full title of the funded effort.

Signal Processing, Pattern Formation and Adaptation in Networks of Neural Oscillators

Grant/Contract Number

AFOSR assigned control number. It must begin with "FA9550" or "F49620" or "FA2386".

FA9550-12-10388

Principal Investigator Name

The full name of the principal investigator on the grant or contract.

Dr. Edward W. Large

Program Officer

The AFOSR Program Officer currently assigned to the award

Dr. Patrick O. Bradshaw

Reporting Period Start Date

08/01/2012

Reporting Period End Date

07/31/2016

Abstract

In this project, we developed a theoretical framework for auditory neural processing and auditory perception. We modeled the auditory system as a dynamical system consisting of oscillatory networks, and auditory perception as stable dynamic patterns formed in the networks in response to acoustic signals. We developed GrFNNs, generic models that capture the neurocomputational properties of a family of neurophysiological models using bifurcation theory. We conducted theoretical analyses of GrFNNs and made significant progress in understanding the signal processing, pattern formation and plasticity in them. We developed three models that exploit these properties to model important aspects of auditory neurophysiology and auditory perception: a model of cochlear dynamics, a model of mode-locked neural oscillation in the human auditory brainstem, and a model of cortical phase locking to auditory rhythms. Future modeling efforts based on canonical dynamical systems could bring us closer to understanding fundamental mechanisms of hearing, communication, and auditory system development. In addition to these accomplishments, we produced a computational framework for GrFNNs in Matlab, sped up our computational simulations using GPU acceleration, and created a C++ version of the GrFNN code to develop end-user applications that run on CPUs, GPU, mobile platforms and embedded devices. We

DISTRIBUTION A: Distribution approved for public release.

anticipate that this computational framework will power the next generation of auditory processing hardware and software.

Distribution Statement

This is block 12 on the SF298 form.

Distribution A - Approved for Public Release

Explanation for Distribution Statement

If this is not approved for public release, please provide a short explanation. E.g., contains proprietary information.

SF298 Form

Please attach your [SF298](#) form. A blank SF298 can be found [here](#). Please do not password protect or secure the PDF. The maximum file size for an SF298 is 50MB.

[Final+Performance+Report+FA95501210388+SF280+1.pdf](#)

Upload the Report Document. File must be a PDF. Please do not password protect or secure the PDF . The maximum file size for the Report Document is 50MB.

[FinalReportV5.pdf](#)

Upload a Report Document, if any. The maximum file size for the Report Document is 50MB.

Archival Publications (published) during reporting period:

New discoveries, inventions, or patent disclosures:

Do you have any discoveries, inventions, or patent disclosures to report for this period?

No

Please describe and include any notable dates

Do you plan to pursue a claim for personal or organizational intellectual property?

Changes in research objectives (if any):

Change in AFOSR Program Officer, if any:

Changed Program Officer from Dr. William Larkin to Dr. Patrick Bradshaw Effective June 6,2014

Extensions granted or milestones slipped, if any:

N/A

AFOSR LRIR Number

LRIR Title

Reporting Period

Laboratory Task Manager

Program Officer

Research Objectives

Technical Summary

Funding Summary by Cost Category (by FY, \$K)

	Starting FY	FY+1	FY+2
Salary			
Equipment/Facilities			
Supplies			
Total			

Report Document

Report Document - Text Analysis

Report Document - Text Analysis

DISTRIBUTIÓN A: Distribution approved for public release.

Appendix Documents

2. Thank You

E-mail user

Oct 31, 2016 17:02:45 Success: Email Sent to: ed@circular-logic.com